Chapter XVIII

BUBBLE INTERACTIONS WITH VORTICES

GEORGES L. CHAHINE
DYNAFLOW, Inc.
7210 Pindell School Road
Fulton, Maryland 20759
U.S.A.

An understanding of the fundamental mechanisms involved in the interaction between bubbles and vortices is relevant to many important engineering applications. Classical assumptions of bubble sphericity and decoupling between bubble and flow behavior prevent one from capturing some essential elements of the interaction. Bubble motion and deformation are seen to be of great importance for most bubbles in the size spectrum. In this chapter, studies on bubble capture by a vortex, bubble motion and deformation during that capture, and bubble behavior once the bubble is on the vortex axis are described. Flow field modifications once the bubble is on the vortex axis are also briefly considered. The most promising approach appears to consist of a coupling between a boundary element method to describe the bubble behavior, and a viscous flow solver to describe the basic flow.

XVIII.1 Introduction

The simultaneous presence of bubbles and vortices is typical of many high velocity turbulent flows. For example, in marine propellers at high rotational speeds, the helical tip vortices formed at the tip of each blade 'cavitate' and become sites of bubble concentration and fluid vaporization into what is termed 'tip vortex cavities' (see photograph in Figure 18.1.1*a*). This phenomenon is addressed in more detail in Chapter XVII. While for practical reasons engineers tend to superficially address the fundamental problem – by stating, for example, that cavity formation in the vortex will occur if the pressure on the centerline drops in the monophase model below the liquid vapor pressure – a closer look at the fundamental processes at work reveals that the actual phenomenon is rather very complex and

S. I. Green (ed.), Fluid Vortices, 783–828.

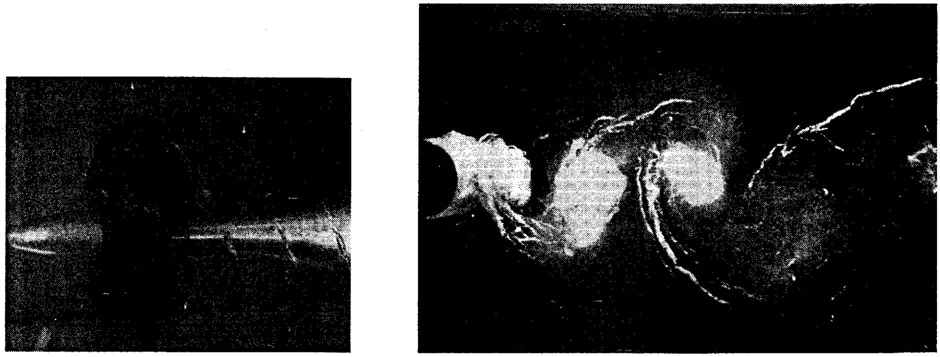

(a) (b)

Figure 18.1.1 Practical examples of bubbles and vortices. a) Tip vortex cavitation on a propeller (Chahine et al. 1993b), b) Vortex cavitation in the separated region behind a cylinder. Courtesy of J.Y Billard, Ecole Navale, Brest, France.

very poorly understood. Questions such as 'How does a microscopic bubble behave in the presence of the vortex?' and 'How and to what extent does the presence of bubbles modify the flow field of the vortex?' have, at this point, only preliminary answers or no answers at all. The interaction between bubbles and vortex flows is in fact of relevance to several fluid engineering problems. Important examples include cavitation in shear layers, boundary layers, tip vortex cavitation, bubbles in the shear layer of submerged jets, cavitation behind orifices, bubbles in separated flow areas (see Figure 18.1.1*b*), microbubbles in boundary layers, etc. In the above mentioned flows, bubbles are held responsible for dramatic effects such as noise generation, materials erosion, and bubble drag reduction. These effects, experimentally observed and widely accepted, are not yet completely understood. Therefore, a satisfactory control of the deleterious effects is not presently possible.

This chapter will try to highlight the problems, present some proposed explanations and methods for solution, and provide some preliminarily confirmed results. However, it does not claim to answer all the complex and presently unanswered questions, and likely fails to address some of the problems that will appear to be important in some configurations in future research.

XVIII.1.1 Mechanistic Description

When a bubble approaches a region of high vorticity in a liquid, it is accelerated towards the center of the vortex (see discussion in Chapter I). The asymmetric pressure field pushes the bubble towards the vortex axis while it is swirling. On its path the bubble experiences a decreasing ambient pressure which can lead to an increase in the bubble size. Simultaneously, since the non-uniformity of the pressure field around the bubble increases with proximity to the vortex axis, bubble shape deformation increases. An explosive bubble growth is provoked if the pressure in the vortex field drops below the bubble '*critical pressure*,' p_c. For a bubble of radius r_o in static equilibrium when the ambient pressure is P_o, this pressure is defined as the pressure below which the bubble cannot be in equilibrium. If one assumes the gas in the bubble expands isothermally (see §4.1, Equation 18.4.3), one may show that this pressure is determined by[1]

$$p_c = P_v - \frac{4\sigma}{3r_c} \tag{18.1.1}$$

where σ is the surface tension parameter, and r_c is the '*critical radius*' given by

$$r_c = \left[\frac{3r_o^3}{2\sigma}\left(P_o - P_v + \frac{2\sigma}{r_o}\right)\right]^{1/2} \tag{18.1.2}$$

where P_v is the liquid vapor pressure (Hammitt 1980).

Over the last decade several investigators have addressed the phenomenon of bubble capture by a vortex (Bovis 1980a,b; Latorre 1982; Ligneul 1989; Ligneul and Latorre 1989). However, these studies made the strong simplifying assumption that the bubble remains spherical as it changes in volume. In addition, they did not consider vortex flow modification by the presence and behavior of the bubble. More recently, Chahine (1990a,b) considered a broader approach where bubble deformation and motion were coupled while neglecting flow field modification by the bubble presence. Chahine showed that the pressure gradient across the bubble can lead to a significant departure from bubble sphericity, and suggested that the deformation and later splitting of the bubble during its motion towards the vortex center is, in addition to its volume change, the main source of noise in vortex cavitation. This bubble deformation appears to explain why tip vortex noise at cavitation inception occurs very close to the blade (Higuchi et al. 1989), and is in agreement with recent observations by Maines and Arndt (1993) about bubble capture in tip vortex cavitation. We will consider the details of the broader approach in the following sections.

One can distinguish three phases in the interactive dynamics of bubbles and vortices: a) bubble capture by the vortex, b) interaction between the vortex and an initially quasi-spherical bubble on its axis, c) dynamics of elongated bubbles on the vortex axis. After some phenomenological and order of magnitude considerations of the phenomena at hand, we will consider each of the three phases and the method of solution proposed for their study.

[1] Obtained by considering Equation (18.4.4), writing $\mathcal{V} = \frac{4}{3}\pi r_b^3$ and $\mathcal{V}_0 = \frac{4}{3}\pi r_0^3$, and solving for the minimum of the function $P_L(r)$.

XVIII.2 Order of Magnitude Considerations

In order to analyze the problem of bubble capture and behavior in a line vortex, let us consider as an example the Rankine vortex flow field described in §I.1. We adopt a notation consistent with that section, denoting Γ as the vortex circulation, and u_θ as the only non-zero velocity component. However, in order to avoid potential confusion with the bubble radius definitions later, we will use R_c for the radius of the viscous core (R is used in §I.1). For distances r smaller than R_c the flow has a solid body rotation behavior (velocities vary as r), while for distances r larger than R_c the flow behaves as in an ideal inviscid irrotational vortex (velocities vary as $1/r$). The expression for the velocity is given by Equation 1.1.15. For such a flow, the pressure field is known and its value $p(r)$ is given by Equation 1.1.17. A key parameter which appears in (1.1.17) is the '*swirl parameter*,' Ω, defined as

$$\Omega = \frac{\frac{1}{2}\varrho\left(\frac{\Gamma}{2\pi R_c}\right)^2}{p_\infty} \tag{18.2.1}$$

Ω characterizes the intensity of the pressure drop due to the rotation, normalized by the ambient pressure, p_∞. To illustrate the importance of this parameter, we divide (1.1.17) by p_∞ to obtain the following normalized expressions for the pressure and the pressure gradient:

$$\begin{aligned} &\overline{p}(\overline{r}) = 1 - \frac{\Omega}{\overline{r}^2} && \frac{\partial \overline{p}}{\partial \overline{r}} = \frac{2\Omega}{\overline{r}^3} && \overline{r} \geq 1 \\ &\overline{p}(\overline{r}) = 1 - \Omega\left(2 - \overline{r}^2\right) && \frac{\partial \overline{p}}{\partial \overline{r}} = 2\Omega\overline{r} && \overline{r} \leq 1 \end{aligned} \tag{18.2.2}$$

with

$$\overline{r} = \frac{r}{R_c} \quad \text{and} \quad \overline{p}(\overline{r}) = \frac{p(r)}{p_\infty} \tag{18.2.3}$$

Note that the pressure on the vortex axis is $(1 - 2\Omega)$ and goes to zero when Ω approaches $1/2$.

As seen in Figure 1.1.5, the pressure gradient steepens in the inviscid region when the viscous core is approached, achieves its maximum at $\overline{r} = 1$, and levels off in the viscous core close to the vortex axis. If a bubble is subjected to the pressure field shown in the figure, it will experience a higher liquid pressure on its right side than on its left side, the difference being greater for larger bubbles. Similarly, the bubble is 'sheared,' since fluid particles on the bubble/liquid interface experience different velocities depending on their location on the bubble. The type of shearing action depends on the position of the bubble relative to the viscous core/inviscid fluid boundary, R_c. If the bubble is fully immersed in the inviscid region of the flow, fluid particles on its left side will experience larger velocities, while if it is fully immersed in the solid body rotation region of the flow, fluid particles on its right side will experience larger velocities. The most complex situation is when the bubble is partly in the viscous core and partly in the inviscid region. In that case, it is expected that the bubble behavior will be vortex flow model dependent, because the sharp separation between the two regions in the mathematical representation does not exist in the physical reality.

Due to the pressure and velocity gradients, the bubble is accelerated toward the axis while growing and deforming. Therefore, depending on its size and position, the bubble experiences a pressure variation along its surface and a slip velocity relative to the surrounding fluid. This results in some degree of bubble shape deviation from sphericity. The importance of this deviation is a function of the relative orders of magnitude of the pressure gradient, the bubble wall acceleration due to volume change, and surface tension forces.

An evaluation of the bubble wall acceleration can be obtained from a characteristic bubble radius, R_b, and from the Rayleigh time, τ_R. The Rayleigh time is the time needed for an empty bubble to collapse from its radius R_b to 0, under the influence of the pressure outside the bubble (Rayleigh 1917). For the present problem let's take the outside local pressure at $r = R_c$ as the characteristic pressure. ($\overline{p} = 1 - \Omega$) is then the typical local ambient pressure, and the Rayleigh time is:

$$\tau_R = R_b \sqrt{\frac{\varrho}{p_\infty(1-\Omega)}} \tag{18.2.4}$$

The characteristic bubble wall acceleration, γ_{growth}, at $r = R_c$ is then:

$$\gamma_{growth}\big|_{r=R_c} \simeq \frac{R_b}{\tau_R^2} \simeq \frac{p_\infty(1-\Omega)}{\varrho R_b} \tag{18.2.5}$$

This value is to be compared with the acceleration force $\gamma_{gradient}$ due to the pressure gradients expressed in (18.2.2):

$$\gamma_{gradient} \simeq \frac{1}{\varrho}\frac{\partial P}{\partial r}$$

$$\gamma_{gradient}\big|_{r=R_c} \simeq \frac{2\Omega p_\infty}{\varrho R_c} \tag{18.2.6}$$

The ratio between these two accelerations can be evaluated, for instance at $r = R_c$, to yield the simple expression:

$$\left.\frac{\gamma_{gradient}}{\gamma_{growth}}\right|_{r=R_c} = \frac{2R_b}{R_c}\cdot\frac{\Omega}{1-\Omega} \tag{18.2.7}$$

This expression highlights the relative importance of the characteristic bubble size R_b, and the viscous core size R_c. Keeping the surface tension parameter the same (see discussion on the Weber number below), the larger the ratio (18.2.7) is, the more important bubble deformation will be. *This remark has important implications concerning scale effects where R_b and R_c do not increase in the same proportion between scale and model,* since in most practical cases bubble distributions and sizes are uncontrolled and typically cannot be scaled much, while the size of the vortical regions depends on the selected geometry and velocity scales.

The ratio (18.2.7) is only an indication of the relative importance of bubble growth and slip forces at a given position. The relative importance of these competing forces changes during the bubble capture process. For instance, the acceleration of the bubble toward the vortex axis increases with its proximity to the viscous core while the growth rate tends toward a constant value (decreasing pressure gradient). This indicates that strong deformation becomes predominant relative to volume change when either the bubble is very close to the axis or the vortex circulation (the "*swirl parameter*", Ω) becomes large.

Another important physical factor which affects bubble shape is the surface tension. A normalized value of the corresponding pressure, a Weber number, can be constructed by combining the surface tension (σ) with either the pressure difference between the inside and the outside of the bubble, or the amplitude of the variations of the local pressures (pressure gradients) around the bubble. The first number, W_{e_1}, is given by:

$$W_{e_1} = \frac{p_i - p_\infty(1-\Omega)}{\sigma/R_b} \tag{18.2.8}$$

where p_i is the pressure inside the bubble. The second number, W_{e_2}, is given by:

$$W_{e_2} = R_b \frac{\partial p/\partial r}{\sigma/R_b} \tag{18.2.9}$$

which can be written for $r = R_c$:

$$W_{e_2} = 2\Omega\left(\frac{p_\infty}{\sigma/R_b}\right)\left(\frac{R_b}{R_c}\right) = W_{e_1}\frac{2\Omega}{\overline{p_i} - (1-\Omega)}\cdot\frac{R_b}{R_c} \tag{18.2.10}$$

For small values of either of these two numbers, surface tension forces are predominant and prevent bubble distortion and deviation from sphericity. Expression (18.2.10) shows that this is possible only if Ω is small and/or if R_b is much smaller than R_c. Therefore, as for the discussion of the acceleration forces, one expects larger bubble deformations for stronger vortex circulations and larger bubbles.

XVIII.3 Bubble Capture by a Vortex

Despite several significant contributions to the study of bubble capture in a vortex, to our knowledge no complete approach has yet been undertaken. While the overall approach, in terms of the investigation of the bubble motion, has several similarities to the problem of the interaction between vortices and solid particles (see Chapter XIX), bubbles, unlike solid particles, will deform and change volume while interacting with the vortex flow field. The complexity of the problem has led the various contributors to neglect one or several of the factors in play, and therefore to only investigate the influence of a limited set of parameters. The first approaches to the problem were attempted independently at about the same time by Bovis (1980a), and Latorre (1980). While both studies accounted for volume change during bubble motion, the basic assumptions and effects taken into account were quite different. Bovis (1980a,b) considered the case where the flow velocities in the vortex flow are large enough to justify the assumptions of inviscid potential flow. This simplification, valid for instance in tip vortex cavitation where very large tangential velocities come into play, and when the bubble is not too close to the vortex axis, allows one to consider other important effects. For instance, one can then consider, in a consistent fashion, important phenomena such as the modification of the vortex flow by the presence of the bubble and the volume change and shape deformation of the bubble (Duraiswami and Chahine 1991). On the other hand, Latorre (1980) and in subsequent studies (Ligneul and Latorre 1989) considered real fluid effects to determine the bubble motion equation, but neglected bubble shape deformation and modification of the flow caused by the bubble. They coupled these equations with a spherical bubble dynamics model to deduce noise emission in tip vortex cavitation.

In the potential flow approach, the expression of the modified flow field due to the presence of a spherical bubble is based on Weiss' theorem (Milne-Thomson 1968). In a spherical system of coordinates centered at the sphere center, if the undisturbed potential flow in the absence of the sphere of radius a is $\Phi_0(r,\theta,\phi)$,the velocity potential of the modified flow due to the presence of the fixed sphere is $\Phi(r,\theta,\phi)$ given by the equation:

$$\Phi(r,\theta,\phi) = \Phi_0(r,\theta,\phi) + \frac{1}{a}\int_0^{a^2/r^2} x\frac{\partial\Phi_0(x,\theta,\phi)}{\partial x}\,dx \tag{18.3.1}$$

Using the notation in Figure 18.3.1, the velocity potential of the vortex flow is:

$$\Phi_0(r,\theta,\phi) = \frac{\Gamma}{2\pi}\tan^{-1}\frac{r\sin\theta\sin\phi}{\zeta(t)+r\sin\theta\cos\phi} \tag{18.3.2}$$

where Γ is the vortex circulation and $\zeta(t)$ is the instantaneous distance between the vortex and the bubble center.

Similarly, the velocity potential of the flow due to the bubble's radius variation in time, $\overset{\circ}{a}(t)$, is

$$\Phi_b(r,\theta,\phi) = -\frac{a^2(t)\,\overset{\circ}{a}(t)}{r} \tag{18.3.3}$$

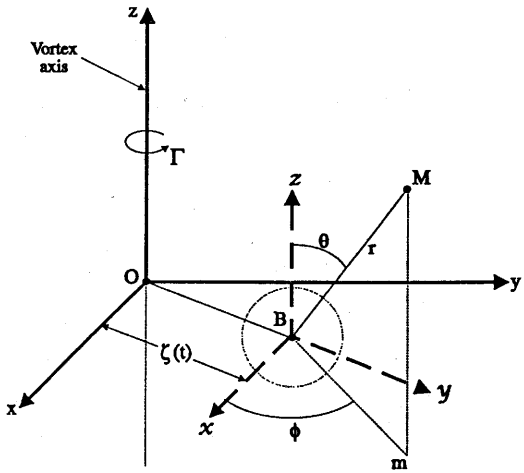

Figure 18.3.1 Sketch of the geometric quantities involved in the analytical description of bubble capture in a vortex line.

where ∘ indicates time differentiation. If we account for a relative velocity $(\mathbf{V} - \mathbf{V_B})$ between the spherical bubble and the fluid, the modified bubble velocity potential becomes:

$$\Phi_b(r,\theta,\phi) = -\frac{a^2(t)\,\mathring{a}\,(t)}{r} - \frac{a^3(t)}{2r^3}\mathbf{r}\cdot(\mathbf{V} - \mathbf{V_B}) \tag{18.3.4}$$

where $\mathbf{V}(\mathrm{t})$ and $\mathbf{V_B}(\mathrm{t})$ are the instantaneous fluid and bubble center velocities. The absolute velocity potential in the fixed coordinate system attached to the vortex, Φ_a, which accounts for bubble motion and radius variations, is then:

$$\Phi_a = \Phi_0 - \frac{a^2\,\mathring{a}}{r} - \frac{a^3}{2r^3}\mathbf{r}\cdot(\mathbf{V} - \mathbf{V_B}) + \frac{1}{a}\int_0^{a^2/r^2} x\frac{\partial\Phi_0(x,\theta,\phi)}{\partial x}dx \tag{18.3.5}$$

The equation of motion of the sphere can now be obtained by using Bernoulli's equation and integrating the pressure over the surface of the sphere. The resulting force leads to the following dynamic equation:

$$\frac{4}{3}\pi a^3\varrho_b\frac{d\mathbf{V_B}}{dt} = \varrho\iint_S\left[\frac{\partial\Phi_a}{\partial t} + \frac{|\nabla\Phi_a|^2}{2}\right]\mathbf{n}ds \tag{18.3.6}$$

where ϱ and ϱ_b are the liquid and bubble content density, a the bubble radius, $\mathbf{n}$ the normal vector to the bubble surface, and $d\mathbf{V_B}/dt$ the bubble acceleration. The evaluation of (18.3.6) in the general case is rather complex. However, a simplified asymptotic expression can be obtained when the radius of the bubble is small relative to the distance from the vortex axis,

$$\epsilon = \frac{a_0}{\zeta_0} \ll 1 \tag{18.3.7}$$

The two nondimensional components of the acceleration are then:

$$\left(\frac{\varrho_b}{\varrho} + \frac{1}{2}\right) \frac{d\overline{V_{br}}}{d\overline{t}} = -\frac{3}{2\overline{\zeta}^3} + \left(\frac{\varrho_b}{\varrho} + \frac{1}{2}\right) \frac{\overline{V_{b\theta}^2}}{\overline{\zeta}} - \frac{\overline{V_{br}}\overline{\overset{\circ}{a}}}{\overline{a}} \tag{18.3.8}$$

$$\frac{d\overline{V_{b\theta}}}{d\overline{t}} = -\frac{\overline{V_{b\theta}}\overline{V_{br}}}{\overline{\zeta}} + \overline{\overset{\circ}{a}} \left(\frac{3}{\overline{\zeta}} - \frac{2\overline{V_{b\theta}}}{\overline{a}}\right) \tag{18.3.9}$$

where the velocities are normalized by the tangential velocity at the location ζ_o of the center of the bubble at $t = 0$, and time by the ratio between the distance ζ_o, and that characteristic velocity,

$$\overline{V_i} = \frac{V_i}{(\Gamma/2\pi\zeta_o)}$$

$$\overline{t} = \frac{t}{(2\pi\zeta_o^2/\Gamma)} \tag{18.3.10}$$

Similarly, ζ is normalized with the initial position, $\overline{\zeta} = \zeta/\zeta_o$. Note that $V_{br} = d\zeta/dt$, and that for a bubble ϱ_b/ϱ is negligible. The third component along ϕ is obviously zero due to the symmetry of the problem (see Darrozes and Chahine (1983), for further discussion and the derivation of the above equations).

In the studies of Ligneul and Latorre (1989) the bubble equation (18.3.6) is replaced by an empirical force balance equation first given by Johnson and Hsieh (1966):

$$\frac{d\mathbf{V_B}}{dt} = 3(\mathbf{V} - \mathbf{V_B})\frac{\overset{\circ}{a}}{a} - \frac{3\nabla p}{\varrho} + \frac{C_d}{4a}|\mathbf{V} - \mathbf{V_B}| \tag{18.3.11}$$

where C_d is a viscous drag coefficient. The first two terms on the right hand side come from inviscid flow considerations and are therefore included more formally and more accurately in Equation (18.3.6). The first term on the right results from the integration in (18.3.6) of the third term in Equation (18.3.5). It reflects the fact that any slip velocity between the bubble center and the surrounding fluid increases with an increase of the bubble wall velocity and a decrease of the bubble radius. Therefore, the bubble center decelerates during bubble growth and accelerates rapidly during the bubble collapse where both $\overset{\circ}{a}$ and a^{-1} are very large. The second term is in fact an acceleration term of the relative or slip velocity, $(\mathbf{V} - \mathbf{V_B})$, whose expression has been often debated in the multiphase flow community (van Wijngaarden 1980). The third term is a viscous drag term where the drag coefficient C_d depends on the Reynolds number of the relative flow, R_{e_b}. Ligneul and Latorre (1989) used the expression:

$$C_d = \frac{24}{R_{e_b}}\left[1 + 0.177R_{e_b}^{0.63} + 2.6 \times 10^{-4} R_{e_b}^{1.38}\right]$$

with

$$R_{e_b} = \frac{2a\,|\mathbf{V} - \mathbf{V_B}|}{\nu} \tag{18.3.12}$$

Other authors add a memory term (Basset term) which accounts for the full history of the slip velocity through an integration between 0 and t. Based on equation (18.3.11) the equations of motion of the bubble become for a Rankine vortex of viscous core radius, R_c:

$$\frac{dV_{br}}{dt} = \zeta V_{b\theta}^2 - 3V_{br}\left[\frac{\mathring{a}}{a} + \frac{C_d\,|\delta V|}{4a}\right] - \frac{3\Gamma^2}{4\pi^2 R_c^2} f_1\left(\frac{\zeta}{R_c}\right)$$

$$\zeta\frac{dV_{b_\theta}}{dt} = -2\,\mathring{\zeta}\,V_{b\theta} + 3\xi\left[\frac{\mathring{a}}{a} + \frac{C_d\,|\delta V|}{4a}\right] \tag{18.3.13}$$

$$\frac{dV_{bz}}{dt} = -3z\left[\frac{\mathring{a}}{a} + \frac{C_d\,|\delta V|}{4a}\right]$$

with

$$|\delta V| = \left(V_{br}^2 + V_{b_\theta}^2 + V_{bz}^2\right)^{\frac{1}{2}}$$

$$\left\{\begin{array}{ll} f_1 = \frac{\zeta}{R_c} & \xi = \frac{\Gamma\zeta}{2\pi R_c^2} - \zeta\frac{dV_{b_\theta}}{dt} \\ f_1 = \frac{\zeta^3}{R_c^3} & \xi = \frac{\Gamma}{2\pi\zeta} - \zeta\frac{dV_{b_\theta}}{dt} \end{array}\right\} \quad \begin{array}{l} \zeta \le R_c \\ \zeta \ge R_c \end{array} \tag{18.3.14}$$

Both approaches (Bovis 1980a; Latorre 1980) used the spherical bubble dynamics equation – known as Rayleigh-Plesset Equation (Plesset 1948) – to determine the bubble radius variation with time:

$$\varrho\left(a\,\overset{\circ\circ}{a} + \frac{3}{2}\,\overset{\circ}{a}^2\right) - 4\mu\frac{\mathring{a}}{a} = -P_\infty(t) + P_v + P_{go}\left(\frac{a_o}{a}\right)^{3k} - 2\frac{\gamma}{a} \tag{18.3.15}$$

In (18.3.15) μ is the dynamic viscosity, P_{go} is the initial gas pressure with k the polytropic gas constant, P_v is the vapor pressure, and γ is the surface tension coefficient. Assumptions leading to this equation are described further in §4.1.

XVIII.3.1 Capture Time

In order to get an idea of the characteristic time for bubble capture by the vortex, let us consider equations (18.3.8) and (18.3.9). If one considers – for an order of magnitude evaluation – the case where the rate of change of the bubble volume is negligible relative to the other terms, then the two equations of motion degenerate to:

$$\mathcal{M}\frac{d\overline{V_{br}}}{d\bar{t}} = -\frac{3}{2\bar{\zeta}^3} + \mathcal{M}\frac{\overline{V_{b\theta}^2}}{\bar{\zeta}}$$
$$\frac{d\overline{V_{b\theta}}}{d\bar{t}} = -\frac{\overline{V_{b\theta}V_{br}}}{\bar{\zeta}} \qquad (18.3.16)$$

where

$$\mathcal{M} = \frac{\varrho_b}{\varrho} + \frac{1}{2} \qquad (18.3.17)$$

Equations 18.3.16 can be integrated to give the position of the non-deforming bubble relative to the vortex axis as a function of time. Using $d\zeta/dt$ as an intermediary variable (expressing d/dt as $d/d\zeta \cdot d\zeta/dt$), and assuming that the bubble center has no initial radial velocity ($v_{ro} = 0$), while the initial tangential velocity is $v_{\theta o}$, Equation 18.3.16 leads to:

$$\overline{V_{b\theta}}(t) = \frac{\overline{v_{\theta o}}}{\bar{\zeta}(\bar{t})} \qquad \text{and} \qquad \bar{\zeta}(\bar{t}) = \left[1 + \left(\overline{v_{\theta o}}^2 - \frac{3}{2\mathcal{M}}\right)\bar{t}^2\right]^{1/2} \qquad (18.3.18)$$

Equation 18.3.18 is very instructive in terms of the motion of a particle of density ϱ_b in a vortex flow field. Depending on the sign of $\left(\overline{v_{\theta o}}^2 - \frac{3}{2\mathcal{M}}\right)$, the particle will be attracted or repelled by the vortex. This term is the difference between inertial (centrifugal) and pressure forces. For bubbles entrained in the flow field of the vortex, $v_{\theta o}$ is between 0 and 1, and $\mathcal{M}$ is very close to $\frac{1}{2}$, since $\varrho_b/\varrho \ll 1$. As a result

$$\bar{\zeta}(\bar{t}) \simeq \sqrt{1 + (\overline{v_{\theta o}}^2 - 3)\bar{t}^2} \geq \sqrt{1 - 3\bar{t}^2} \qquad (18.3.19)$$

The capture time, T_c, for a bubble initially at rest in the fluid ($\overline{v_{\theta o}}(0) = 0$) is therefore approximately

$$\bar{t}_c = \sqrt{\frac{1}{3}} \qquad \text{or} \qquad T_c = \frac{2\pi\zeta_o^2}{\Gamma\sqrt{3}} \qquad (18.3.20)$$

In fact, for a sphere, only viscous effects can be responsible for bubble entrainment with the flow, since with the inviscid model Equation 18.3.6 clearly indicates that only radial forces on the sphere are non-zero. In the presence of viscosity, friction forces enable entrainment of the bubble by the fluid. The characteristic time of viscous effects (the order of magnitude of the time needed for bubble entrainment by the flow) is

$$T_\nu = \frac{a_o^2}{\nu} \qquad (18.3.21)$$

The qualitative nature of the bubble capture depends on the relative size between T_c and T_ν.

If $T_c \gg T_\nu$ the capture time is long. Viscous effects are strong enough for the bubble to be entrained relatively rapidly by the liquid and it starts swirling around the vortex while approaching the vortex axis very slowly.

If $T_c \ll T_\nu$ the opposite situation occurs: viscous effects are very slow to take effect and the bubble is practically sucked into the vortex moving towards its center in an almost purely radial fashion.

Finally, for $T_c \approx T_\nu$ entrainment by the liquid and attraction towards the center of the vortex occur on the same time scale. Therefore, the bubble approaches the axis in a spiral fashion.

The above reasoning allows one to define a '*violent capture radius*' around the vortex that is bubble radius dependent. A bubble of radius a_o will be sucked in by the vortex if it is within the radial distance $R_{capture}$:

$$R_{capture} = a_o \sqrt{\frac{\Gamma\sqrt{3}}{2\pi\nu}} \tag{18.3.22}$$

XVIII.4 Numerical Study

Numerical methods presently offer the best hope for solutions to the bubble-vortex interaction problem. Coupled with guidance from analytical, experimental and order of magnitude or phenomenological studies, a numerical approach can minimize the number of physical phenomena that need to be considered. One of the numerical methods that has proven to be very efficient in solving the type of free boundary problem associated with bubble dynamics is the Boundary Element Method. Among others, Guerri et al. (1981), Blake et al. (1986, 1987), and Wilkerson (1989) used this method in the solution of axisymmetric problems of bubble growth and collapse near boundaries. This method was extended to three-dimensional bubble dynamics problems by Chahine et al. (1988, 1989). We describe here the model, then apply it to the case of bubbles in a vortex flow.

XVIII.4.1 Bubble Flow Equations

Let us consider the cases where the presence of a bubble in the flow has significant effects, that is cases where bubble volume variation in time is not negligible. For such cases the bubble wall velocity is large but subsonic. Therefore, one can neglect viscosity and compressibility effects on the bubble dynamics. These assumptions, classical in cavitation bubble dynamics studies, result in a potential flow (velocity potential, Φ) which satisfies the Laplace equation,

$$\nabla^2\Phi = 0 \tag{18.4.1}$$

The solution must in addition satisfy initial conditions and boundary conditions at infinity, at the bubble walls and at the boundaries of any nearby bodies.

At all moving or fixed surfaces (such as a bubble surface or a nearby boundary) an identity between fluid velocities normal to the boundary and the normal velocity of the boundary itself is to be satisfied:

$$\nabla\Phi \cdot \mathbf{n} = \mathbf{V_s} \cdot \mathbf{n} \tag{18.4.2}$$

where $\mathbf{n}$ is the local unit vector normal to the bubble surface and $\mathbf{V_s}$ is the local velocity vector of the moving surface.

The bubble is assumed to contain noncondensible gas as well as the vapor of the surrounding liquid. The pressure within the bubble is considered to be the sum of the partial pressures of the noncondensible gases, P_g , and that of the liquid vapor, P_v. Vaporization of the liquid is assumed to occur fast enough that the vapor pressure remains constant and equal to the equilibrium vapor pressure at the liquid ambient temperature. In contrast, since time scales associated with gas diffusion are much larger, the amount of noncondensible gas inside the bubbles is assumed to remain constant and the gas is assumed to satisfy the polytropic relation,

$$P_g \mathcal{V}^k = constant \tag{18.4.3}$$

where $\mathcal{V}$ is the bubble volume and k the polytropic constant. $k = 1$ for isothermal behavior and $k = c_p/c_v$ for adiabatic conditions.

The pressure in the liquid at the bubble surface, P_L, is obtained at any time from the following pressure balance equation:

$$P_L = P_v + P_{g_0} \left(\frac{\mathcal{V}_0}{\mathcal{V}}\right)^k - \mathcal{C}\sigma \tag{18.4.4}$$

where P_{g_0} and $\mathcal{V}_0$ are the initial gas pressure and volume respectively, σ is the surface tension, $\mathcal{C}$ is the local curvature of the bubble, and $\mathcal{V}$ is the instantaneous value of the bubble volume. In the numerical procedure P_{g_0} and $\mathcal{V}_0$ are known quantities at $t = 0$.

XVIII.4.2 Boundary Integral Method for Three-Dimensional Bubble Dynamics

In order to simulate single and multiple bubble behaviors in complex flow configurations, including the full non-linear boundary conditions, a three-dimensional Boundary Element Method was developed and implemented by Chahine et al. (1988-1991). The Boundary Element Method was chosen here because of its computational efficiency. Considering only the boundaries of the fluid domain reduces the dimensions of the problem by one. This method is based on Green's equation which provides Φ anywhere in the domain of the fluid (field points P) if the velocity potential, Φ , and its normal derivatives are known on the fluid boundaries (points M), and if Φ satisfies the Laplace equation:

$$\iint_S \left[-\frac{\partial \Phi}{\partial n}\frac{1}{\mid \mathbf{MP} \mid} + \Phi\frac{\partial}{\partial n}(\frac{1}{\mid \mathbf{MP} \mid})\right] ds = a\pi\Phi(P) \qquad \textbf{(18.4.5)}$$

where $a\pi = \Omega$ is the solid angle under which P sees the fluid.

a = 4, if P is a point in the fluid,
a = 2, if P is a point on a smooth surface, and
a < 4, if P is a point at a sharp corner of the surface.

If the field point is selected to be on the surface of any of the bubbles or on the surface of the nearby boundaries, then a closed set of equations can be obtained and used at each time step to solve for values of $\partial\Phi/\partial n$ (or Φ), assuming that all values of Φ (or $\partial\Phi/\partial n$) are known at the preceding step.

To solve Equation 18.4.5 numerically, it is necessary to discretize each bubble into panels, perform the integration over each panel, and then sum up the contributions to complete the integration over the entire bubble surface. To do this, the initially spherical bubbles are discretized into a geodesic shape using flat, triangular panels. This discretization of a bubble shape is described in Chahine et al. (1988 and 1993c). Equation 18.4.5 then becomes a set of N equations (N is the number of discretization nodes) of index i of the type:

$$\sum_{j=1}^{N}\left(A_{ij}\frac{\partial \Phi_j}{\partial n}\right) = \sum_{j=1}^{N}(B_{ij}\Phi_j) - a\pi\Phi_i \qquad i = 1,..,N \qquad \textbf{(18.4.6)}$$

where A_{ij} and B_{ij} are elements of matrices which are the discrete equivalents of the integrals given in Equation 18.4.5.

To evaluate the integrals in (18.4.5) over any particular panel, a linear variation of the potential and its normal derivative over the panel is assumed[2]. In this manner, both Φ and $\partial\Phi/\partial n$ are continuous over the bubble surface, and are expressed as a function of the values at the three nodes which delimit a particular panel. The two integrals in (18.4.5) are then evaluated analytically. The resulting expressions, too long to present here, can be found in Chahine et al. (1988).

In order to proceed with the computation of the bubble dynamics, several quantities appearing in the above boundary conditions need to be evaluated at each time step. The bubble volume presents no particular difficulty, while the unit normal vector, the local surface curvature, and the local tangential velocity at the bubble interface need further development. In order to compute the curvature of the bubble surface a three-dimensional local bubble surface fit, $f(x,y,z) = 0$, is first computed. The unit normal at a node can then be expressed as:

[2] Obviously, higher order descriptions are conceivable, and would probably improve accuracy at the expense of additional analytical effort and numerical computation time.

$$\mathbf{n} = \pm \frac{\nabla f}{|\nabla f|} \tag{18.4.7}$$

with the appropriate sign chosen to ensure that the normal is always directed towards the fluid. The local curvature is then computed using

$$\mathcal{C} = \nabla \cdot \mathbf{n} \tag{18.4.8}$$

To obtain the total fluid velocity at any point on the surface of the bubble, the tangential velocity, $\mathbf{V_t}$, must be computed at each node in addition to the normal velocity, $\mathbf{V_n} = \partial\Phi/\partial n\ \mathbf{n}$. This is also done using a local surface fit to the velocity potential, $\Phi_l = h(x, y, z)$. Taking the gradient of this function at the node considered, and eliminating any normal component of velocity appearing in this gradient, gives a good approximation for the tangential velocity

$$\mathbf{V_t} = \mathbf{n} \times (\nabla\Phi_l \times \mathbf{n}) \tag{18.4.9}$$

The basic procedure can then be summarized as follows. With the problem initialized and the velocity potential known over the surface of the bubble, an updated value of $\partial\Phi/\partial n$ can be obtained by performing the integrations in (18.4.5) and solving the corresponding matrix equation 18.4.6. $D\Phi/Dt$ is then computed using a 'modified' Bernoulli equation (see Equation 18.4.17 below). Using an appropriate time step, all values of Φ on the bubble surface can then be updated using Φ at the preceding time step and $D\Phi/Dt$,

$$\frac{D\Phi}{Dt} = \frac{\partial\Phi}{\partial t} + \left(\frac{\partial\Phi}{\partial n}\mathbf{n} + \mathbf{V_t}\right) \cdot \nabla\Phi \tag{18.4.10}$$

In the results presented below, the time step, dt, was based on the ratio between the length of the smaller panel side, l_{min}, and the highest node velocity, V_{max}. This choice limits the motion of any node to a fraction of the smallest panel side. It has the great advantage of constantly adapting the time step, by refining it at the end of the collapse – where l_{min} becomes very small and V_{max} very large – and by increasing it during the slow bubble size variation period. New coordinate positions of the nodes are then obtained using the displacement:

$$d\mathbf{M} = \left(\frac{\partial\Phi}{\partial n}\mathbf{n} + V_t\mathbf{e}_t + \mathbf{V_o}\right) dt \tag{18.4.11}$$

where $\mathbf{n}$ and $\mathbf{e}_t$ are the unit normal and tangential vectors. This time stepping procedure is repeated throughout the bubble growth and collapse, resulting in a shape history of the bubble.

XVIII.4.3 Pressure/Velocity Potential Relation

Let us consider the case of a bubble growing and collapsing in a nonuniform flow field ('*basic flow*') of velocity $\mathbf{V}_0$ that is known and satisfies the Navier-Stokes equations:

$$\frac{\partial \mathbf{V}_0}{\partial t} + \mathbf{V}_0 \cdot \nabla \mathbf{V}_0 = -\frac{1}{\varrho}\nabla P_0 + \nu \nabla^2 \mathbf{V}_0 \tag{18.4.12}$$

Also assume that in presence of the oscillating bubbles, the resulting velocity field, given by $\mathbf{V}$, also satisfies the incompressible Navier-Stokes equation:

$$\frac{\partial \mathbf{V}}{\partial t} + \mathbf{V} \cdot \nabla \mathbf{V} = -\frac{1}{\varrho}\nabla P + \nu \nabla^2 \mathbf{V} \tag{18.4.13}$$

Both $\mathbf{V}$ and $\mathbf{V}_0$ also satisfy the continuity equation. We can now define bubble flow velocity and pressure variables, $\mathbf{V}_b$ and P_b, as follows:

$$\mathbf{V}_b = \mathbf{V} - \mathbf{V}_0 \qquad P_b = P - P_0 \tag{18.4.14}$$

If we consider the case where the '*bubble flow*' field is potential[3] :

$$\mathbf{V}_b = \nabla \Phi_b \qquad \nabla^2 \Phi_b = 0 \tag{18.4.15}$$

and subtract (18.4.12) from (18.4.13) accounting for (18.4.15) we obtain

$$\nabla \Psi = \nabla \left[\frac{\partial \Phi_b}{\partial t} + \frac{1}{2} \mid \mathbf{V}_b \mid^2 + \mathbf{V}_0 \cdot \mathbf{V}_b + \frac{P_b}{\varrho} \right] = \mathbf{V}_b \times (\nabla \times \mathbf{V}_0) \tag{18.4.16}$$

The assumption of a *potential* '*bubble flow*' implies that, even though the basic flow is allowed to interact with the bubble dynamics and be modified by it, in this model no new vorticity can be generated by the bubble behavior. Equation 18.4.16 can be integrated to obtain an equation similar to the classical unsteady Bernoulli equation. For the particular case of the vortex line flow, Equation 18.4.17 can always be written in cylindrical coordinates:

$$\frac{\partial \Psi}{\partial z} = 0$$

In this case the Bernoulli equation is to be replaced by:

$$\frac{\partial \Phi_b}{\partial t} + \frac{1}{2} \mid \mathbf{V}_b \mid^2 + \frac{P - P_0}{\varrho} = \textit{constant in the axial direction} \tag{18.4.17}$$

[3] This is obviously a simplifying assumption that needs to be removed in future research on the subject. §8 presents a first step in that direction.

Accounting for conditions at infinity, the pressure in the liquid at the bubble wall, P_L, given by (18.4.17), is related to Φ_b and the pressure field in the Rankine vortex P_0 by:

$$\left[\frac{P_L}{\varrho} = \frac{P_0}{\varrho} - \frac{\partial \Phi_b}{\partial t} - \frac{1}{2} \mid \mathbf{V}_b \mid^2\right]_{at\ bubble\ wall} \tag{18.4.18}$$

XVIII.4.4 Specialization to Axisymmetric Problems

In axisymmetric problems, the physical variables (velocity potential and pressure) are independent of the angular coordinate. Thus, the angular coordinate only enters the formulation through the argument of the Green's function in Equation 18.4.5.

$$G(\mathbf{MP}) = 1/ \mid \mathbf{MP} \mid \tag{18.4.19}$$

The integration of these dependent quantities can be explicitly carried out. Let C represent the trace in a meridian plane of the geometry under consideration. Let r, θ, z be the cylindrical coordinates of point M, a point on the boundary, and without loss of generality we select the coordinates of P to be $(R, 0, Z)$. The integral equation (18.4.5) can then be written

$$\phi(R,0,Z) = \int_C \phi(r,z) r \frac{\partial}{\partial n_M}\left(\int_0^{2\pi} G d\theta\right) ds_M - \int_C \frac{\partial \phi}{\partial n_M} r \int_0^{2\pi} G d\theta ds_M \tag{18.4.20}$$

In writing the above expression the fact that the normal to an axisymmetric surface is independent of the angular coordinate has been used. Thus, integration over the angular variable is reduced to evaluation of one integral

$$I = \int_0^{2\pi} G(r,\theta,z;R,Z) d\theta = -\frac{1}{4\pi}\int_0^{2\pi} \frac{d\theta}{\sqrt{R^2 + r^2 - 2rR\cos\theta + (Z-z)^2}} \tag{18.4.21}$$

which is nothing but the *complete elliptic integral of the first kind,* $K(m)$, with

$$m = \frac{4rR}{A} \qquad A = \sqrt{(R+r)^2 + (Z-z)^2} \tag{18.4.22}$$

The equation for the potential may then be written as:

$$2\pi\phi(R,Z) = -\int_C \phi(r,z) r \frac{\partial}{\partial n_M}\left(\frac{4K(m)}{\sqrt{A}}\right) ds_M + \int_C \frac{\partial \phi}{\partial n_M}(r,z)\frac{4K(m)}{\sqrt{A}} r ds_M \tag{18.4.23}$$

Further details of the method can be found in Taib (1985).

XVIII.5 Numerical Results and Discussion

XVIII.5.1 Validation of Numerical Codes

The use of the Boundary Element Method to study axisymmetric bubble dynamics has been validated by the various authors quoted earlier. This has included both comparisons with a quasi-analytical solution for spherical bubbles (Rayleigh-Plesset Equation 18.3.15) and experimental validation for the relatively simple cases of spherical and axisymmetric bubble collapse near flat solid walls. Figures 18.5.1*a* and 18.5.1*b* show comparative results between the codes used below (axisymmetric **2DynaFS** and fully three-dimensional **3DynaFS**) and the semi-analytical results.

Comparison of the results of the 3D code against previously published results, for the relatively simple cases shown below, have been very favorable. For spherical bubbles, comparison with the Rayleigh-Plesset "exact" solution revealed that numerical errors for a "coarse" discretization of a 102-node bubble (not shown in the above figures) was about 2 percent of the achieved maximum radius, but was very small, 0.03 percent, of the bubble period. The error on the maximum radius was less than 0.14 percent for a discretized bubble of 162 nodes (320 panels), and dropped to 0.05 percent for 252 nodes (500 panels). Comparisons were also made with studies of axisymmetric bubble collapse available in the literature (Guerri et al. 1981; Blake et al. 1986, 1987), and have shown, for the coarse discretization, bubble periods that differ from these studies by about 1 percent. Finally, compar-

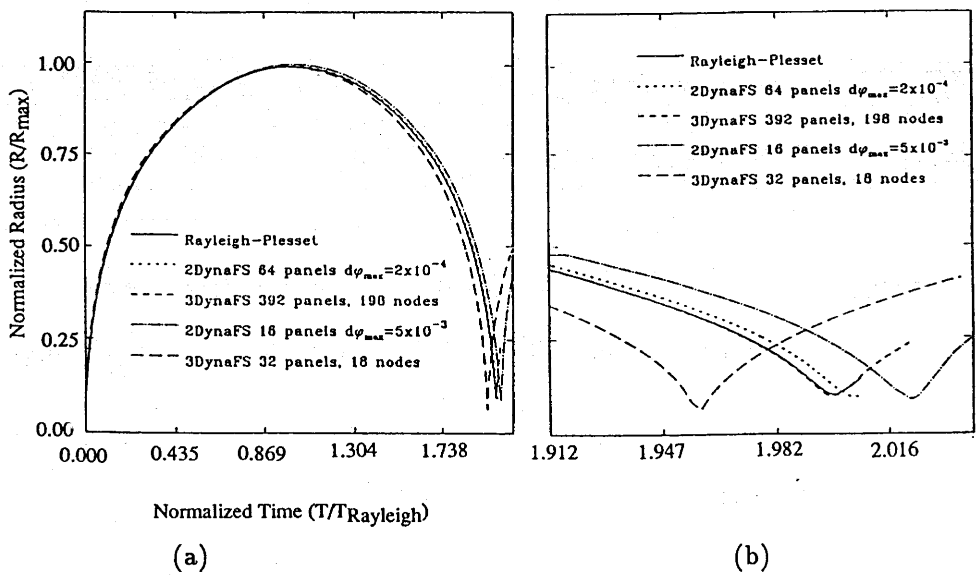

Figure 18.5.1 Comparison between Rayleigh-Plesset solution and the axisymmetric BEM code **2DynaFS** and the 3D BEM code **3DynaFS**. Computations started with an initial bubble pressure 584 times larger than the ambient pressure. a) Over bubble period. b) End of collapse.

ison with actual test results of the complex three-dimensional behavior of a large bubble collapse in a gravity field near a cylinder shows very satisfactory results (Chahine 1988, 1991).

XVIII.5.2 Bubble Capture

XVIII.5.2.1 Large Bubble Growth Rate, Low Surface Tension Case

As expected from the mechanistic considerations of §1.1 and §1.2, numerical simulations using the fully three-dimensional numerical approach reveal the potential for large bubble deformations during capture by a vortex. The numerical results indicate that this is the case for a very wide range of bubble sizes and initial values of the pressure difference between the inside and the outside of the bubble.

Figure 18.5.2 shows three-dimensional bubble behavior in the case where the ratio between the pressure inside the bubble and the ambient pressure is significantly large, $p_i/p_\infty = 584.3$. This would be the case where the bubble in equilibrium in a high ambient pressure environment is suddenly subjected to the flow field of a vortex, as for instance when a propeller tip vortex suddenly captures a cavitation bubble (Maines and Arndt 1993; Green 1991). In a Cartesian system of coordinates, $OXYZ$, the bubble is initially centered at (0,0,0), and the line vortex is located parallel to the Z axis, at $\overline{X} = X/R_{max} = 2$ (two times the maximum size, R_{max}, the bubble would have if allowed to grow under the same pressure difference in an infinite medium). The core size considered here is $4R_{max}$. With this geometry the bubble center remains in the plane $Z = 0$.

Figure 18.5.2*b* gives a projected view of the bubble in the XOY plane at different instants. The observer is looking down on the XOY plane from very far on the Z axis. The bubble is seen spiraling around the vortex axis (perpendicular to the figure) while approaching it. At the same time, due to the presence of the pressure gradient, the bubble deforms strongly and a re-entrant jet is formed directed towards the axis of the vortex, thus indicating the presence of a much larger dynamic pressure on the bubble side opposite to the vortex axis.

Figure 18.5.2*a* shows projected views of the same bubble in the YOZ plane seen from the OX axis. Some moderate elongation of the bubble is observed along the axis of the vortex, as well as a very distinct side view of the re-entrant jet. *This result is totally contrary to the common belief that bubbles constantly grow during their capture until they reach the axis, and then elongate along the axis.*

The motion in the XOY plane of two particular points on the bubble, A and B (initially located along OY), are shown in Figure 18.5.3. Also shown is the motion of the midpoint, C. While C seems to follows a path similar to the classical logarithmic spiral, A and B can follow more complicated paths, even moving away from the vortex axis at some point in time for case (b) where the vortex axis was initially at $X = 1$.

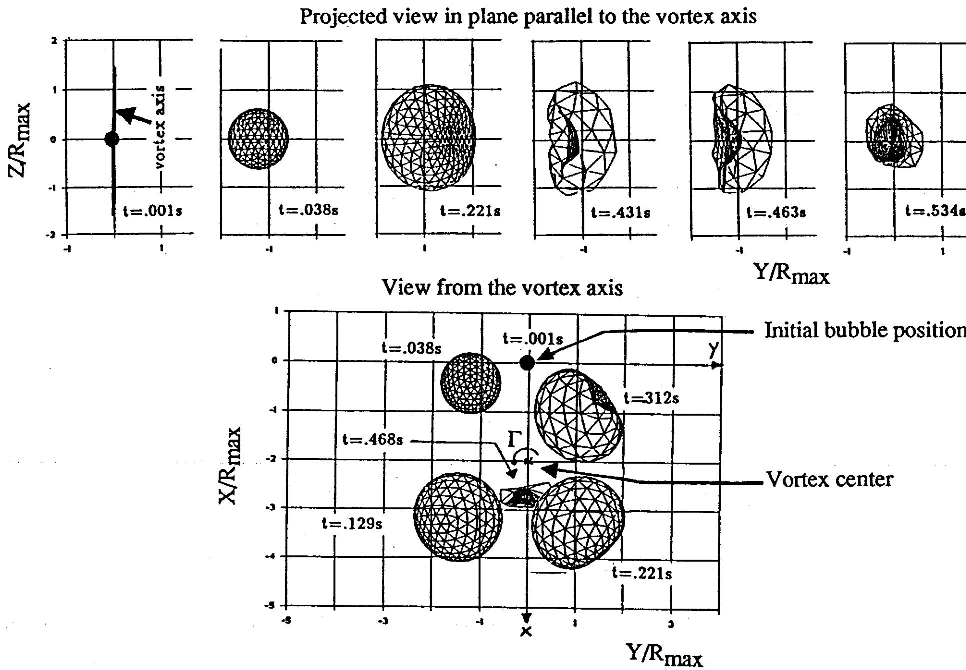

Figure 18.5.2 3D bubble shapes at various times. Bubble initially at the origin of the Cartesian coordinate system, and vortex at $X = 2R_{max}$. $\Omega = 0.474$, $p_i/p_\infty = 584.3$, $R_c/R_{max} = 4$. Projected view (a) (top row) in the ZOY plane; (b) (bottom row) in the XOY plane.

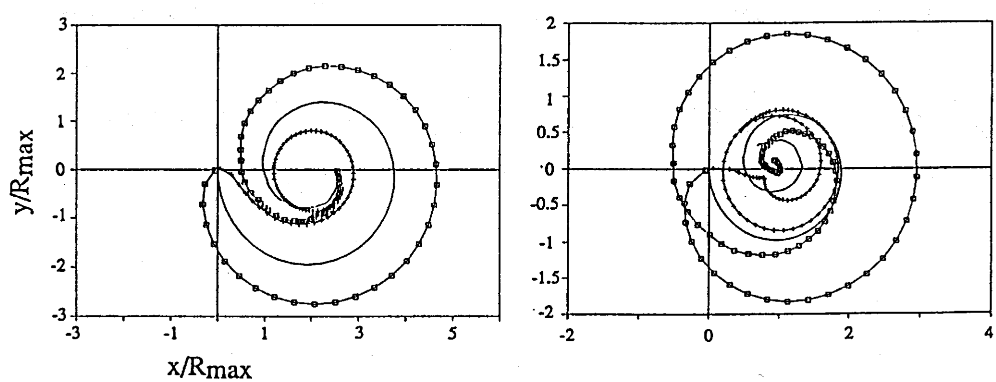

Figure 18.5.3 Motion of the two points initially on axis OX, A and B, and the mid point C between A and B, versus times. $\Omega = 0.474$, $p_i/p_\infty = 584.3$, $a_c/R_{max} = 4$. Vortex located at (a) left: $X = 2R_{max}$; (b) right: $X = R_{max}$.

XVIII.5.2.2 Small Growth Rate and Surface Tension

Figure 18.5.4 considers the influence of bubble size on bubble behavior during the capture process. In all three cases shown in the figure a ratio between the pressures inside and outside the bubble equal to one is considered, $p_i/p_\infty = 1$. In all cases, the viscous core radius is chosen to be $R_c = 2.2\ mm$, while the initial distance between the vortex center and the center of each bubble is chosen to be $\zeta_o \simeq 1.5R_c = 3.2$ mm. The dimensions shown are normalized values with the initial bubble radius for each case. The circulation in the vortex is chosen to correspond to a practical value ($\Gamma = 0.152m^2/s$) for the case of a tip vortex behind a foil, such as that used in the experiments described by Maines and Arndt (1993) and Green (1991). Three bubble sizes are considered: 10 μm, 100 μm and 1000 μm. As expected, bubble deformation increases with the bubble size. The deformation is small for a_o=10 μm, becomes very significant for a_o=100 μm, and is extremely important for a_o=1000 μm. In all cases, the bubbles, while remaining in the inviscid region, are seen to be sheared very strongly by the flow. The smaller bubbles appear to deform in the expected way in a shear flow. The computations were stopped when significant bubble shape deformations necessitated finer time steps. The larger bubble case (a_o=1000 μm) shows extreme bubble elongation and wrapping around the viscous core region.

XVIII.5.3 Multiple Bubbles

One of the key questions that one needs to address in bubble/vortex interaction practical studies is how a distribution of bubbles modifies the flow field in a vortex

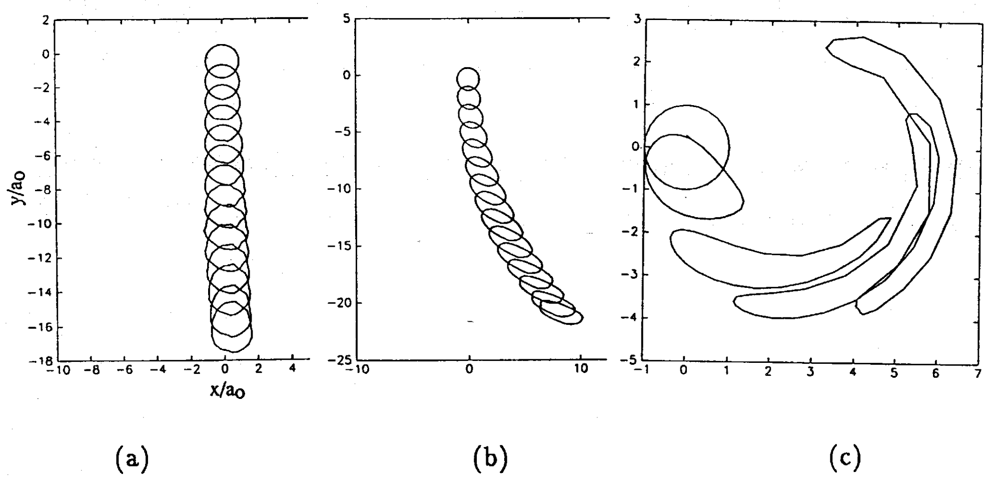

Figure 18.5.4 Bubble contours at various times. $\Gamma = 0.1527m^2/s$, $p_i/p_\infty = 1$, $a_c = 2.2mm$, vortex located at $X = 3.2mm$, with a_o = a) 10μm, b) 100μm, c) 1000μm.

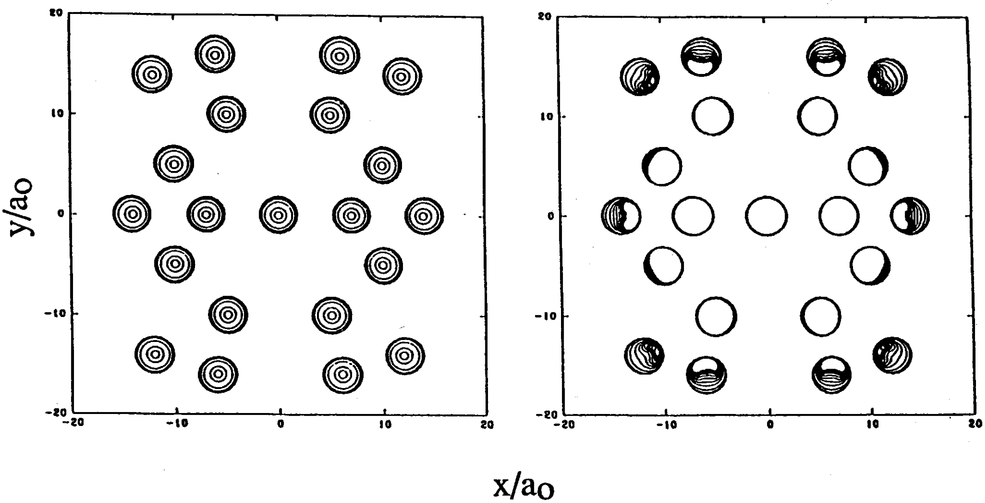

(a) (b)

Figure 18.5.5 Simulation of the dynamical interactions between a cloud of 21 bubbles using 3DynaFS on a Cray. Two planes of symmetry are used. Each bubble has 102 nodes and 200 panels. a) Growth. b) Collapse.

line. In order to address such a problem, the program **3DynaFS** is being modified for effective implementation on a supercomputer. One of the difficulties of such a study is the required large number of discretization points, which prevents lengthy simulations on typical memory and speed limited computers. Figure 18.5.5 shows the behavior of a field of bubbles in the absence of a vortex field, run on a Cray machine. In the case shown in the figure, two planes of symmetry were assumed to minimize computational times. In the presence of a vortex line, use of such a symmetry is not warranted since, due to the varying rates of rotation of each bubble in the vortex field, the symmetry is not preserved during the bubble motion. In addition, due to the high shear rates that bubbles can experience, a relatively large number of discretization points is needed to describe each bubble.

Figure 18.5.6 shows the case of a 5-bubble configuration in the flow field of a line vortex. This run has the advantage of including both vortex/bubble and bubble/bubble interactions. All five bubbles are chosen such that in absence of the vortex flow field, the pressures inside and outside each bubble are the same and equal to 0.74 atm, $p_i/p_\infty = 1$. The viscous core radius and the circulation are again chosen to be in the same ranges as those in the experiments described by Maines and Arndt (1993), and Green (1991). The viscous core is chosen to be $R_c = 2.2mm$, while $\Gamma = 0.1573\ m^2/s$, $\Omega = 0.872$. The initial bubble centers are selected to be on OY axis at the coordinates: $Y = 0, 2, 3, 4$ and $5\ mm$. The vortex line is parallel to the OX axis and is centered on $Y = 1.5\ mm$. As a result, bubbles 1, 2 and 3

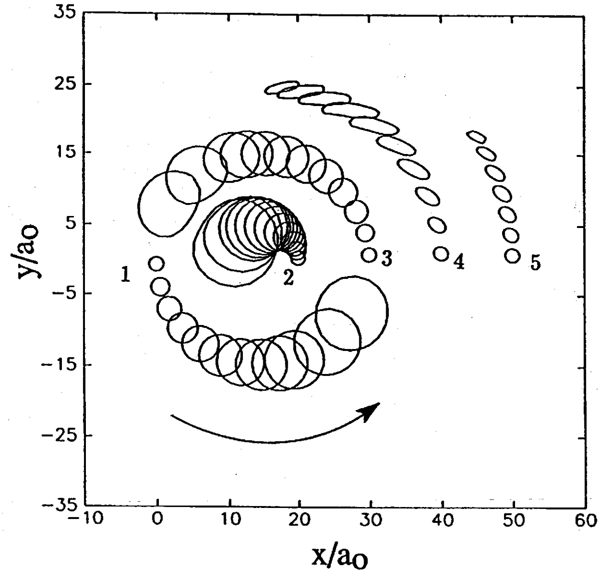

Figure 18.5.6 Dynamical behavior of 5 bubbles in a vortex line flow - bubble contours at various times. The vortex line is perpendicular to the page and centered on $Y = 1.5mm$. $R_c = 2.2mm$, $\Gamma = 0.1573m^2/s$. $\Omega = 0.872$. All bubbles have $a_0 = 100\mu m$.

are initially located in the viscous core, while bubbles 4 and 5 are located in the inviscid flow region. All five bubbles considered have an initial radius of 100 μm. Figure 18.5.6 shows contours of the bubbles as they rotate around the vortex axis at various times. This figure clearly shows the presence of a nonuniform flow field. Indeed, bubble 3, which is the closest to the region of highest angular velocity of the ' *basic flow,*' is seen to swirl around the vortex center at the fastest rate, while bubble 2, which is the closest to the vortex center, is seen to practically rotate around itself. Similarly, the highest shear is seen to occur close to the viscous core edge where the pressure gradients and their variations are steepest.

Since all bubbles were chosen to have the same initial radius and internal pressure, the natural period of oscillation of each of the selected bubbles increases with the proximity to the vortex axis. As a result, the farthest bubble from the axis, Bubble No. 5, collapses first while stretching and deforming. In order to be able to continue the computation following break up of a bubble, that bubble was removed and the computation was continued with the bubbles left.

Figure 18.5.7 shows two three-dimensional views of the bubbles before the collapse of bubble 1. These views enable one to have a better idea of the bubble shape deformation and elongation during the capture phenomenon.

Figure 18.5.8 is a previously unpublished photo of a bubble in the viscous core of the trailing vortex of a hydrofoil (see Green (1991) for details of the experiment).

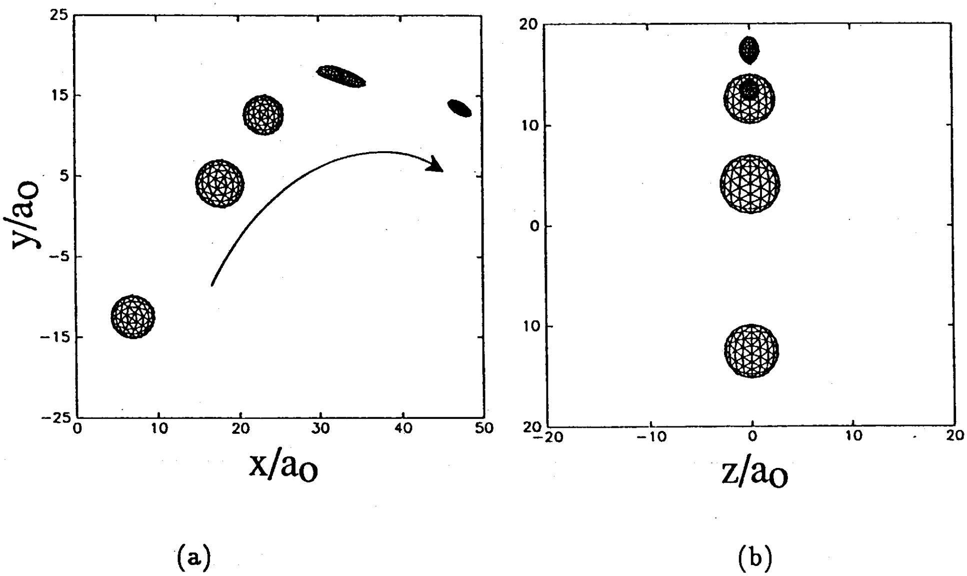

Figure 18.5.7 3D bubble shapes in the vortex line flow field of Figure 18.5.6 before collapse of bubble No. 1. View from (a) OZ axis, (b) OX axis.

The photograph is a double exposure, the time of separation between the two pictures being 150 μs. The three bubble shapes in the top of the figure are aligned along the axis of the vortex. The diameter of these shapes is of the order or 200 μm. The bottom two shapes are those of the same bubble at two instants in time separated by 150 μs, and illustrate very clearly the large deformations of the bubble during its capture by the vortex. As in the numerical simulations presented above, this behavior appears to be related to the large shear stresses experienced by the bubble while approaching the vortex axis. In the first of the two pictures the bubble is very elongated due to shear, while 150 μs later, it appears to have grown in size, due to the pressure drop in the vortex, while conserving a strong deformation on its downstream surface.

XVIII.5.4 Bubble on Vortex Axis

Let us now consider the case where the bubble is placed at the vortex axis at $t = 0$ and starts to grow due to the difference between the internal pressure and the local ambient pressure. Such a problem was considered earlier by Crespo et al. (1990) who studied the dynamics of an elongated bubble. Unfortunately, his model neglected essential elements in the bubble/line vortex dynamics: i.e. the presence of an azimuthal velocity flow field, a rotational and viscous flow, and a pressure "well" on the axis. Crespo obtained a strong jet which initiated at both extreme

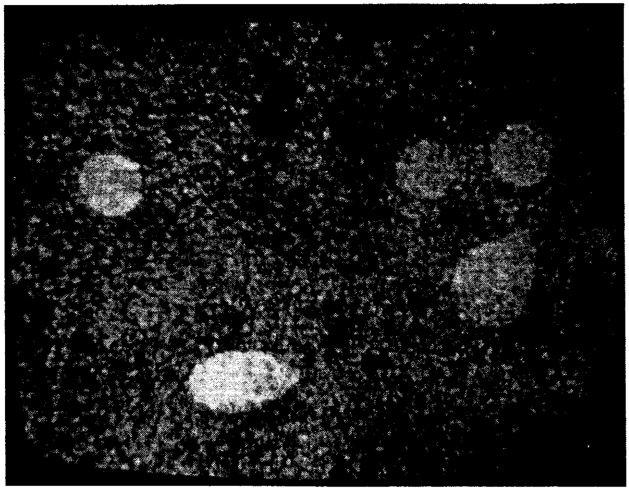

Figure 18.5.8 Double exposure photo of a bubble in the viscous core of the trailing vortex of a NACA 66-209 hydrofoil (see Green 1991). Time of separation between two exposures =150 μs. Scale 170 μm/cm. The three bubble images at the top are of bubbles on the vortex centerline. The two images at the bottom are successive images of one bubble being driven by the centripetal pressure gradient onto the vortex centerline. $R_e = 6.8 \times 10^6$, $\Gamma = 0.232 m^2/s$. Courtesy of Professor S. I. Green, UBC, Canada.

points of the bubble along the axis of symmetry. As shown in Figure 18.5.9a such a behavior is reproduced using the program **2DynaFS** when the vortex flow field is neglected. However, the opposite effect is in general observed when the rotation in the vortex flow is included. Figure 18.5.9b illustrates this for particular values of the circulation, Γ, (or the swirl parameter, Ω) and the normalized core radius, $\overline{R_c} = R_c/R_{max}$. Modifications in the results when Ω and $\overline{R_c}$ are changed are discussed in the following paragraph.

In both cases shown in Figures 18.5.9a and 18.5.9b, the initial bubble shape elongation ratio (the ratio of bubble length to radius) was three. It is clear from the comparison that the swirl flow has a profound effect on the bubble dynamics. Bubble surface portions away from the vortex axis experience much higher pressures than bubble surface portions on and close to the vortex axis, and therefore move much faster during the collapse phase. This difference in collapse rate generates a constriction in the mid-section of the bubble instead of the sharp jets on the axis shown in Figure 18.5.8. The hourglass-shaped bubble then separates into two tear-shaped bubbles.

In Figures 18.5.10$a-c$, the dynamics of initially spherical bubble positioned at $t = 0$ on the vortex axis are studied. The initial internal pressures inside the bubbles are taken to be larger than the pressure on the vortex axis, and the bubbles are left free to adapt to this pressure difference. The figures indicate that the bubble

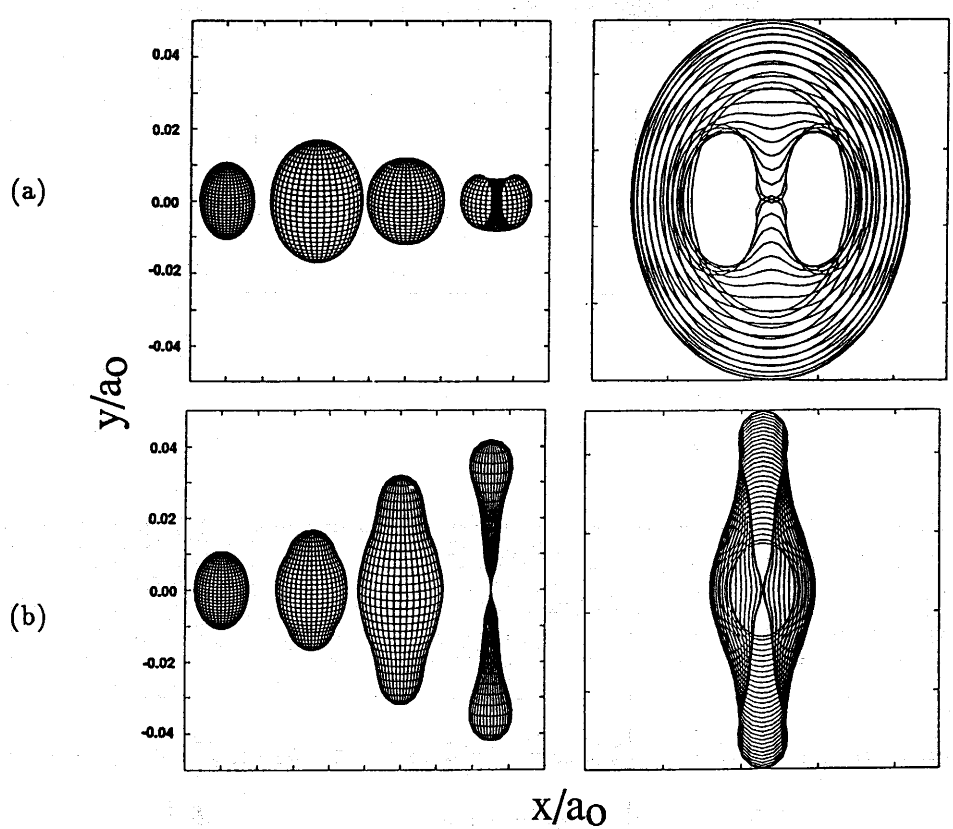

Figure 18.5.9 Comparison between the contours of an elongated bubble during its collapse in the absence and in the presence of swirl. Initial elongation ratio of 3. $p_\infty/p_i = 3.27$. a) No swirl. b) $\Omega = 0.56$. $R_c/R_{max} = 3$.

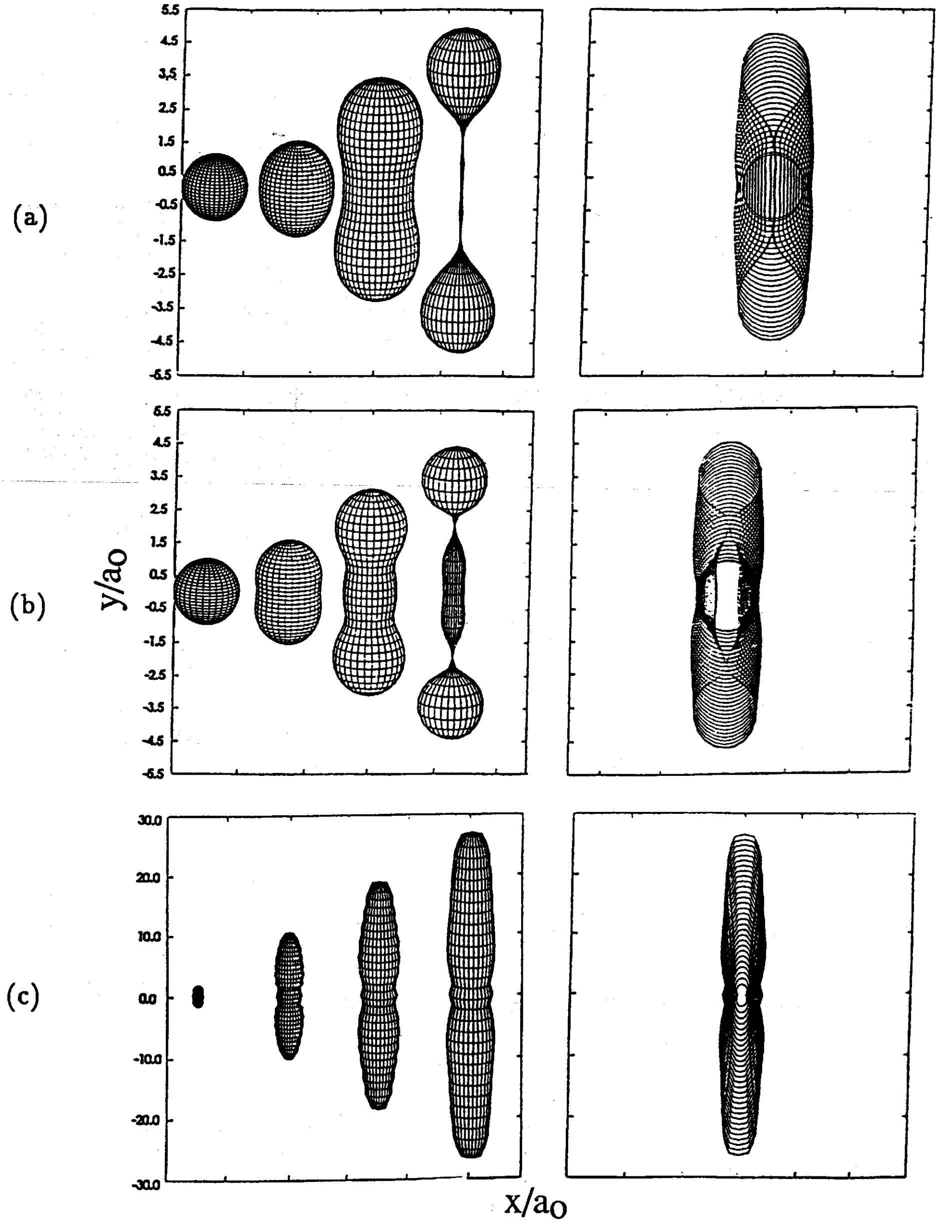

Figure 18.5.10 Bubble dynamics on the axis of a vortex line. Left side shows 3D shapes at selected times. Right side shows bubble contours at increasing times. $\Gamma = 0.005m^2/s$, $R_o = 100\mu m$. a)$p_i/p_\infty = 2$, $R_c/R_o = 1$, b) $p_i/p_\infty = 2$, $R_c/R_o = 1$, c) $p_i/p_\infty = 1$, $R_c/R_o = 0.57$.

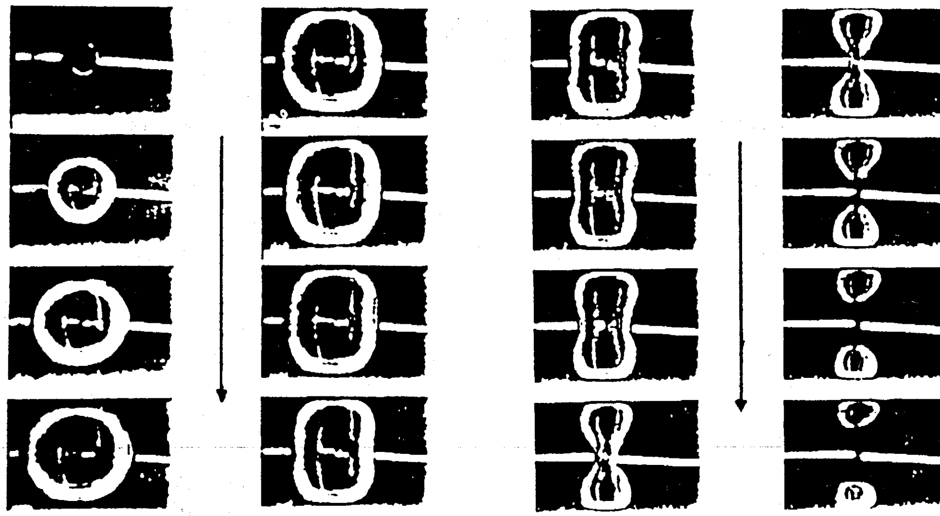

Figure 18.5.11 Bubble collapse between two solid parallel plates resulting in the formation of an hourglass-shaped bubble and a line vortex perpendicular to the two plates.

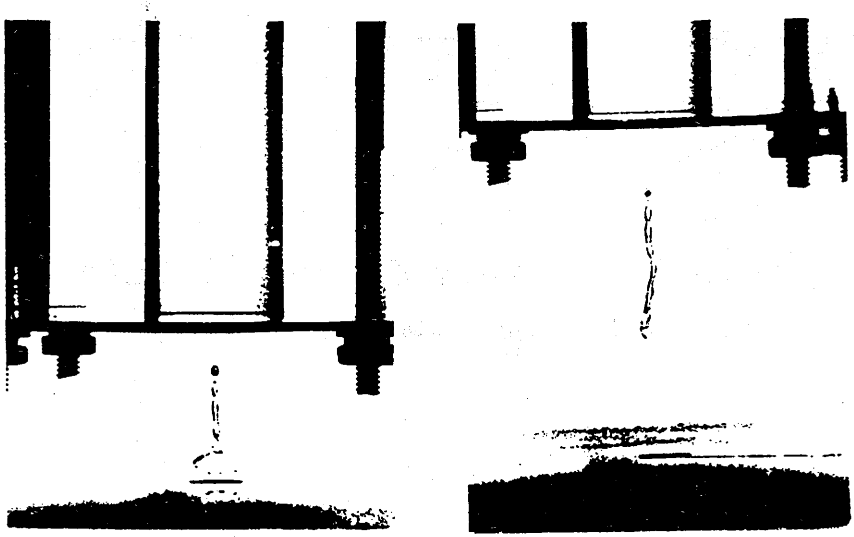

Figure 18.5.12 Cavitation bubble shapes observed at the exit of a vortex tube.

behavior depends significantly, for a given value of the swirl parameter, Ω, on the normalized core radius $\overline{R_c}$. In all cases where the bubble maximum radius, R_{max}, is larger than R_c it appears that the bubble tends to adapt to the vortex tube of radius R_c. This could lead to various bubble shapes, as shown in the following figures, ending up with a very elongated bubble with a wavy surface for large values of R_{max}/R_c.

Figures 18.5.10$a-c$ show bubble contours at various times during growth and collapse for increasing values of the core radius, R_c, and decreasing values of p_i/p_∞. Also shown are selected 3D shapes of the bubbles at various times, which have the advantage of being much more descriptive. It is apparent from these figures, that during the initial phase of the bubble growth, radial velocities are large enough to overcome centrifugal forces and the bubble first grows almost spherically. Later on, the bubble shape starts to depart from spherical and to adapt to the pressure field. The bubble then elongates along the axis of rotation. Once the bubble has exceeded its equilibrium volume, bubble surface portions away from the axis – high pressure areas – start to collapse, or to return rapidly towards the vortex axis. Points near the vortex axis do not experience rising pressures during their motion, are not forced back towards their initial position, and continue to elongate along the axis. As a result, a constriction appears in the mid-section of the bubble. The bubble can then separate into two or more tear-shaped bubbles. It is conjectured that this splitting of the bubbles is a main contributor to cavitation inception noise. This behavior is very similar to that observed for bubble growth and collapse between two plates (Chahine 1989), which results in the formation of a vortex line (Figure 18.5.11)!

Keeping Ω constant while reducing the vortex core size R_c has the effect of steepening the radial pressure gradient along the bubble surface and increasing the rotation speed inside the viscous core. These effects increase the centrifugal force on the fluid particles closer to the vortex axis, which in turn increases the elongation rate of the bubble and results in more and more complex shapes of the elongated bubbles. The bubble can then become subdivided into three, four, or more satellite bubbles during the collapse. The elongated and wavy shapes obtained have been observed in unpublished tests that we have conducted on cavitation on the axis of the vortex formed in a vortex tube (Figure 18.5.12).

XVIII.5.5 Bubble on Vortex Axis Near a Wall

Figures 18.5.13$a-c$ show the collapse of a bubble trapped in a line vortex perpendicular to a solid wall at various distances from this wall. The boundary is at $y = 0$ and its distance to the initial bubble center, L, is normalized with R_{max}. The presence of the wall is accounted for by the incorporation of an image bubble. The uneventful growth phase ends with the elongated spheroid shaped contours shown at the center of each figure. Then, the overall bubble behavior appears to be similar to that in absence of the wall; namely, bubble elongation along the axis followed by a splitting into two bubbles. The presence of the wall is felt by

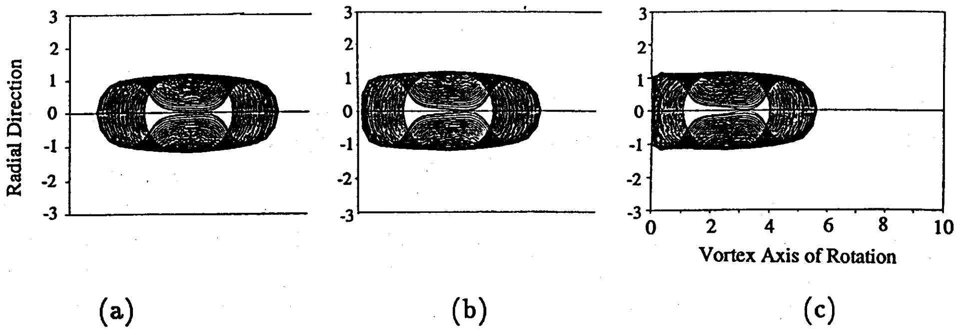

Figure 18.5.13 Influence of solid wall distance on bubble collapse in a line vortex. $\Omega = .475$, $p_i/p_\infty = 584$, $a_c = 1.18$. a) $L/R_{max} = 4$; b) $L/R_{max} = 3$; c) $L/R_{max} = 2.5$.

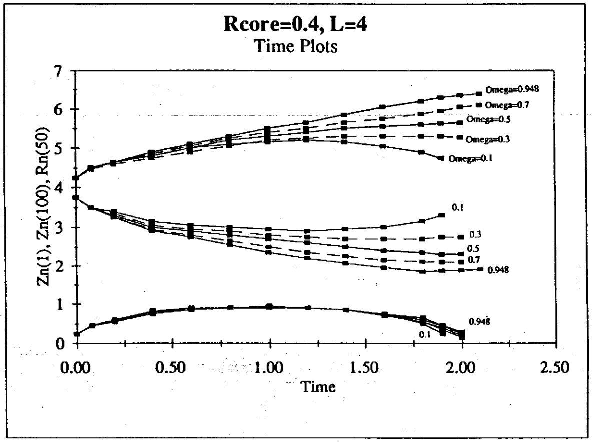

Figure 18.5.14 Influence of Ω on the motion of bubble axial and longitudinal dimensions versus time for a bubble trapped in a line vortex perpendicular to a solid wall. Distances are normalized with R_{max} and times are normalized with the Rayleigh time. $p_i/p_\infty = 584$, $a_c/R_{max} = 0.4$, $L/R_{max} = 4$.

an asymmetry between the two secondary bubbles. In all cases, computation was stopped at bubble splitting. A special treatment to the bubble shape discretization needs to be done after that point (panel removal) and is being implemented. It is speculated, based on previous bubble dynamics observations, that very strong jets that will bring back the two pointed tips (in the splitting region) of the two secondary bubbles will be generated following bubble splitting. This phenomenon is expected to be stronger for the secondary bubble close to the wall since that bubble has a much more elongated tip.

Figure 18.5.14 shows the influence of the circulation parameter, Ω, on the bubble behavior for fixed values of the core radius and the distance to the wall. This figure contains significant information on the scaling of bubble behavior in a vortex flow. Three characteristic dimensions of the bubble are shown as a function of time.

These are the bubble radius along the plane perpendicular to the line vortex, R_n, and the distances between the initial bubble center and the two extreme points on the vortex axis, $Z_n(1)$ and $Z_n(100)$. Figure 18.5.14 shows time variation of these three quantities normalized with R_{max}. Time is normalized with the Rayleigh time based on R_{max} and the pressure difference between P_{go} and the pressure on the vortex axis. It is apparent from this figure that R_n follows the classical Rayleigh model. Variations of Ω between 0.1 and 0.94 modify the normalized bubble period by less than 10 percent. One should notice, however, that bubble period is here defined as the time needed for the bubble to subdivide into two secondary bubbles, and that no bubble surface instability, as described earlier, occurred in that case. Bubble elongation, on the other hand, depends strongly on Ω, as can be seen from the Z_n curves. The elongation of the bubble part close to the wall is seen to be affected for large values of Ω.

XVIII.6 Validation Study: Bubble Interaction with a Vortex Ring

XVIII.6.1 Experimental Study

In order to validate the numerical studies on bubble/vortex interactions, a fundamental experimental and numerical study was conducted. This consisted of the controlled observation of the interaction between a vortex ring and a bubble. The results of the experiment were then compared with those obtained with the 3D free surface dynamics numerical code **3DynaFS** described above (Chahine et al. 1993a).

A vortex ring was generated in a Plexiglas tank using a cylinder equipped with a 2.5 cm radius piston. The cylinder has an sharp lip exit to enhance the roll up of the fluid vortex generated at the lip. This results in a vortex ring with a diameter slightly larger than that of the cylinder (Kalumuck and Chahine 1990). The water in the tank is degassed using a vacuum pump and a spark generated bubble is produced using two tungsten electrodes submerged in the tank which can be manipulated from outside the tank to be placed where desired. The spark is produced by discharging during a very short time period ($\simeq 10^{-4}s$) a high voltage (6000 volts) from a series of capacitors. The interaction between the generated ring and bubble was then observed. A spark generating the bubble has the advantage of simulating cavitation bubbles and allowing one to choose precisely when and where the bubble is generated, which is essential to coordinating the positions of the bubble and the ring, and the starting time of a high speed camera. A triggering line allows one to synchronize the departure of the piston and the triggering of the spark generator using pressure transducers to precisely detect the vortex ring motion. As the piston starts to move down, a pressure pulse is created in the tank by the fluid impulsive motion. This is detected by the transducer probe and

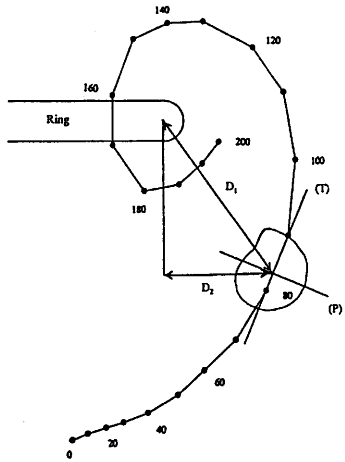

Figure 18.6.1 Particle trajectory around the ring viscous core.

amplified to trigger a delay generator. The output signal (a very short pulse) then triggers the spark generator. Visualization was performed using a HYCAM II high speed camera capable of 11,000 frames per second.

On several of the motion pictures taken very small gas bubbles were present under the piston. The visualization of the motion of these bubbles allows one to observe their trajectory around the vortex ring. The existence of a "viscous core" was apparent from the velocity profile obtained by tracing the microbubbles' motion, whether or not the vortex ring was cavitating. For the cavitating cases, the "viscous core" surrounded the vaporous/gaseous core. A typical trajectory of the small bubbles is shown in Figure 18.6.1. Also shown in this figure is a sketch of a bubble and the particle trajectory line (T). Figure 18.6.1 also shows the geometric characteristics of the bubble/ring positions. D_1 is the distance between the bubble center and the viscous core center when the bubble is at its maximum volume and has the equivalent maximum radius $R_{\max}$. D_2 is the horizontal distance between the bubble and the center of the viscous core. The normalized quantities $\overline{D_1} = D_1/R_{\max}$ and $\overline{D_2} = D_2/R_{\max}$ characterize the bubble/vortex ring interactions. As expected, it is observed that smaller $\overline{D_1}$ and $\overline{D_2}$ correspond to stronger interactions and larger bubble deformations.

Figure 18.6.2a – c drawn in the ring reference frame shows the bubble motion and deformation with time for three selected cases of increasing bubble/shear interaction. The electrodes position shown on each graph is the one at the instant of the spark generation. The vortex ring side view indicates the position of the reference frame.

As can be seen from the pictures in Figure 18.6.3a and from the contours in Figure 18.6.4a, the bubble remains practically spherical during its growth. The

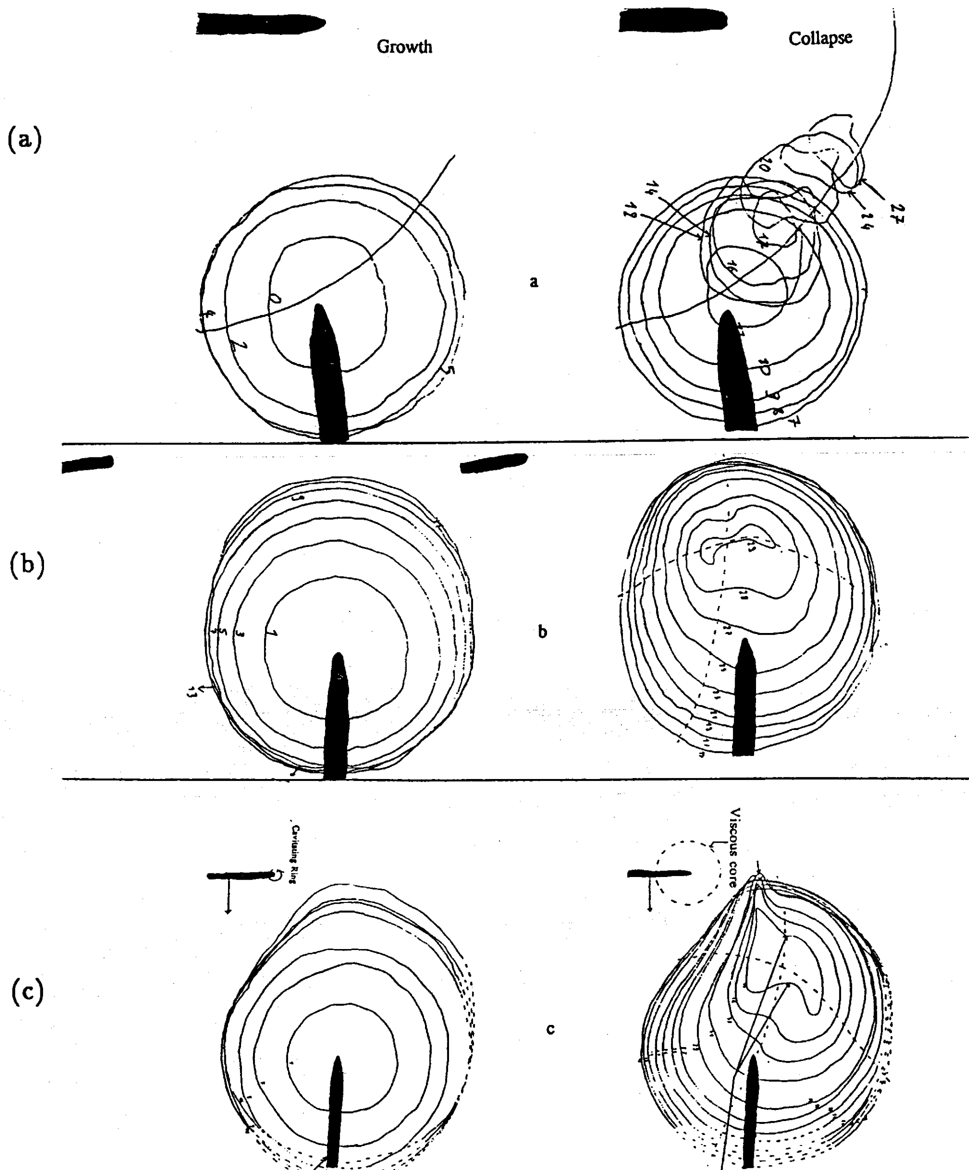

Figure 18.6.2 Bubble contours at various times from the high speed sequences of Figure 18.6.3. a) $\overline{D_1} = 2.16$, $\overline{D_2} = 0$, $V_{ring} = 0.28 m/s$, b) $\overline{D_1} = 2.38$, $\overline{D_2} = 1.5$, $V_{ring} = 0.78 m/s$, c) $\overline{D_1} = 1.1$, $\overline{D_2} = 0.37$, $V_{ring} = 0.82 m/s$.

interaction is weak due to the relatively large distance between the bubble and the ring, and also due to the relatively small circulation of the ring. The first collapse is too fast, and no significant deformation of the bubble is seen until the rebound when a re-entrant jet appears on the bottom face of the bubble followed after the rebound by an outgoing jet on the top face. It appears that during the first bubble oscillation period the bubble translation velocity is smaller than the vortex generated fluid velocity. The bubble therefore sees a flow moving upward. The jet direction (including the re-entrant and the outside jet) is on a pathline of shear flow, and the bubble motion after the collapse follows a particle path line while oscillating and cutting itself in two.

In Figure 18.6.3*b* the bubble first grows spherically, then it starts to stretch into an ovoid shape: the bottom face is less curved and the top face is more curved than in the spherical case. Here the distance $\overline{D_1}$ is not too different from the previous case but the circulation in the vortex ring is about three times larger. When the bubble volume decreases, the stretching due to the shearing action becomes more pronounced and a constriction along the bubble periphery appears along the pathlines (T). The bubble then rebounds with a dumbbell shape.

In Figure 18.6.3*c* the bubble appears to be stretched more and more in the direction of the pathline during its growth, with the top region more stretched than the bottom one, and the top right part growing more than the left one. When the bubble collapses, its left side continues to be sheared by the flow into a pathline direction and a 'beak' forms at the top left part and becomes more pronounced once the volume of the bubble starts to decrease. Then, there is a constriction all around the bubble which appears first on the top face of the bubble. The bubble then cuts itself in two and rebounds as two side-by-side distorted bubbles (or bubble clouds). The left one then touches the cavitating ring and splits again into two parts. The deformations of the bubble are more significant in this case than in the two previous cases, because the bubble is closer to the center of the ring core and experiences a strong shear flow. In addition, there appears to be a "venturi effect" between the bubble and the viscous core that further increases the stretching of the left part of the bubble.

Within the margin of errors of the measurements, comparison of the time variation of the average radius of each bubble shows no significant effect of the presence of shear on the bubble period. However, indications of a lengthening effect of the bubble period can be seen in the characteristic distances between the bubble 'center' and the two upstream and downstream points, along a particle pathline. This effect, however, seems small in the cases presented here and should be investigated further.

XVIII.6.1.1 Physical Explanations

The observations made above can be qualitatively understood by considering the velocity and pressure fields around the bubble. The motion of each point on the surface of the bubble is the result of the combination of the underlying (shear)

(a)

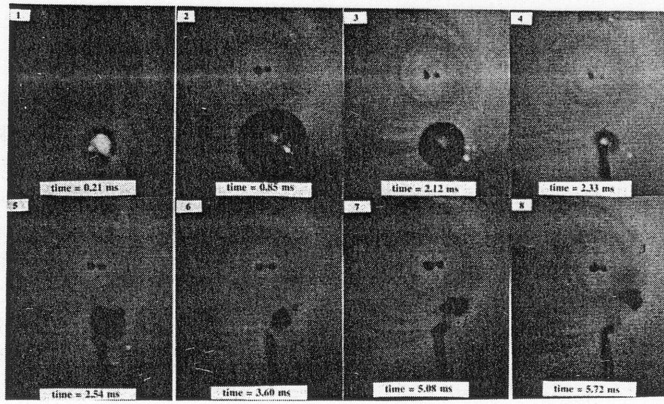

(b)

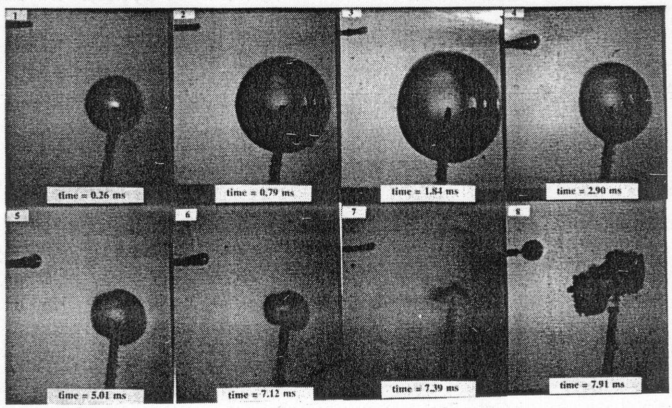

(c)

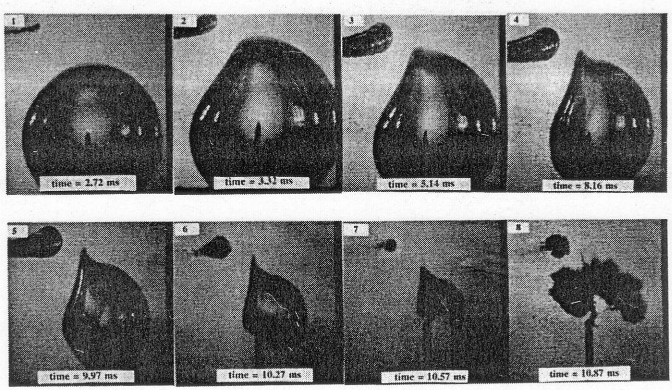

Figure 18.6.3 High speed movie sequences of bubble/vortex ring interaction. a)$\overline{D_1} = 2.16$, $\overline{D_2} = 0$, $V_{ring} = 0.28 m/s$, b) $\overline{D_1} = 2.38$, $\overline{D_2} = 1.5$, $V_{ring} = 0.78 m/s$, c)$\overline{D_1} = 1.1$, $\overline{D_2} = 0.37$, $V_{ring} = 0.82 m/s$.

fluid velocity and of the velocity due to the bubble growth or collapse. The effect of the underlying fluid flow (whose characteristic speed is about $2m/s$) is minor during initial bubble growth and later bubble collapse phases, but becomes most important at the end of the growth and at the beginning of the collapse where bubble wall velocities reach a minimum. Indeed, right after the spark generation, the speed of each point of the bubble surface is very high (about $40m/s$). It then decreases to zero at about the maximum radius, and then increases during the bubble collapse. For a bubble in a uniform flow, the existence of the flow influences the bubble shape by producing a larger bubble growth in the downstream direction and by flattening the bubble shape in the upstream direction. Later on, due to inertia, the downstream part that has extended further collapses faster forming a re-entrant jet directed upstream in the plane of symmetry of the bubble.

When the flow is not uniform, a similar phenomenon occurs but is stronger on one side of the bubble than on the other due to the typical asymmetry of a shear flow. In addition, the possibility that the underlying shear flow becomes, at some point during the bubble history, stronger than the bubble wall velocity creates the possibility of a jet generated by the underlying flow, which can be opposite to the one described above and directed downstream. In the case of the figures shown here, the velocity profile seen by the bubble decreases from left to right. When the bubble starts to grow, the speed of each point is much more important than the velocity of the fluid flow: the bubble is therefore almost spherical. Then, when the speed of each point decreases, the influence of the fluid flow increases. The top part of the bubble grows more than without the presence of the basic flow and, due to the shear, the left part grows more than the right. In addition, the top face is more stretched than the bottom face because on the top face the speeds add up, while they subtract on the bottom. The opposite is true during the collapse where velocities add up on the bottom part of the bubble and subtract on the top.

As the fluid flow moves upward in the case shown in the figure, the re-entrant jet is expected to appear on the top face. However, due to the strong shear, the left part of the bubble is prevented from collapsing. This in turn forces a compensating middle-of-the-bubble constriction, with a tendency to form re-entrant jets on both ends of the bubble along the pathline. This constricted shape of the bubble is similar to that obtained with a bubble collapsing between two walls.

XVIII.6.2 Numerical Modeling

In order to model the bubble/shear flow interaction described above, the Boundary Element Method (BEM) code described above, **3DynaFS**, was used. The flow field of the moving vortex ring was modeled using the following classical expression for the velocity potential at the point M produced by a vortex ring $(\mathcal{R})$:

$$\phi(M) = -\frac{\Gamma}{4\Pi} \iint_{S_R} \frac{\mathbf{e_t} \cdot \mathbf{PM}}{|\mathbf{PM}|^2} ds_R \qquad (18.6.1)$$

where $S_{\mathcal{R}}$ is any surface limited by the vortex ring line ($\mathcal{R}$), and $\mathbf{e}_t$ is the tangential direction along ($\mathcal{R}$). This enables one to determine the velocity and pressure field outside of the viscous core region of the vortex ring.

Figure 18.6.4$a-c$ shows simulation results for the same conditions as the experiment of Figure 18.6.3c. As in the experiment, Figure 18.6.4c shows elongation of the left side of the bubble in the shear flow direction. The formation of a beak at the end of the bubble growth is also evident but not as pronounced as in the experiment. Later a constriction in the bubble shape along the fluid pathline is also apparent. The overall comparison between this numerical modeling and the experiment is encouraging. However, the strong shearing effect on the beak, which prevents the bubble top from collapsing from the left side, is not definitively reproduced in the numerical simulation. This discrepancy is probably because the simulation neglected the vortex *bubble* ring behavior and did not include any modification of the flow due to the growth of the ring bubble near the spark-generated bubble, creating the venturi effect we mentioned earlier.

At the smaller circulations, the tendency of the bubble to elongate and then cut itself into two is also clearly apparent, as in the experiments.

(a)

(b)

(c)

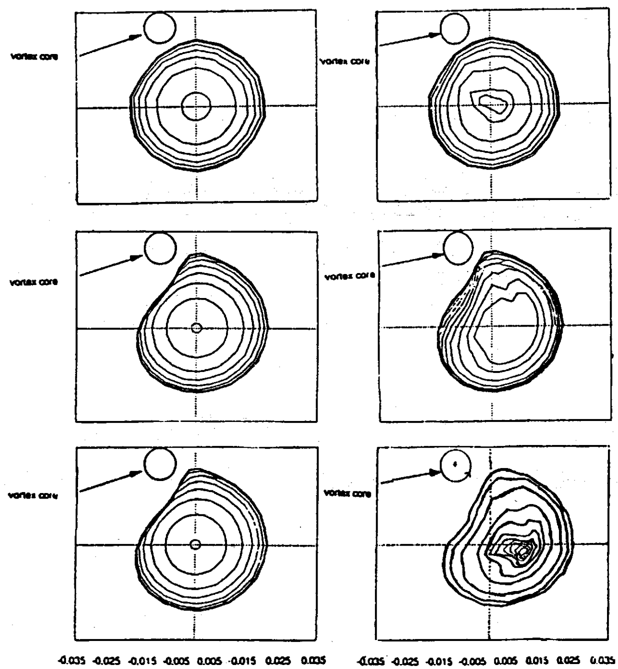

Figure 18.6.4 Numerical simulations of bubble/vortex ring interaction. $\overline{D_1} = 1.1$, $\overline{D_2} = 0.37$, $V_{ring} = 0.82 m/s$. a) $\Gamma = 0.025 m^2/s$; b) $\Gamma = 0.10 m^2/s$; c) $\Gamma = 0.12 m^2/s$, which corresponds to Figure 18.6.3c.

XVIII.7 Other Relevant Studies

One other relevant aspect of bubble/vortex interactions concerns the case where the gaseous phase or cavitation is so developed that the vortex center is filled with gas or vapor. The dynamics of such cavities have been considered in the particular cases of cavitating vortex rings and well developed tip vortices. As for the studies presented above, various simplifying assumptions were made by the various authors in order to address these problems. For the sake of brevity we will not consider these studies here. However, we refer the readers to the following publications on cavitating vortex rings (Chahine and Genoux 1983; Genoux and Chahine 1984; Chahine and Kalumuck 1988; Kalumuck and Chahine 1990). Concerning elongated developed tip vortices, the readers can consult the following publications (Bovis 1980a; Ligneul and Latorre 1989; Ligneul 1989). Current activities in the dynamics of bubbles and mixing layers include work by Reutsch and Meiburg (1991), Kumar and Williams (1991), Rightley and Lasheras (1991), Dvila-Martin et al. (1991), and Stewart and Crowe (1993).

XVIII.8 Full Viscous Interaction Between a Cylindrical Bubble and a Line Vortex

One weakness of the numerical approaches presented above is the fact that, while the influence of the flow on the bubble was fully accounted for, the modification of the flow by the bubble's presence and dynamics was restricted to the case where the 'bubble flow' was potential (see §4.3). In the present section, we will remove this restriction in the simple but interesting case of the interaction between a cylindrical bubble and a line vortex. This corresponds to cases such as described in the previous section, where the line vortex has the central part of its viscous core gaseous or vaporous. As illustrated below, such an analysis is important to determine criteria for unstable bubble growth (cavitation inception), and to describe how bubble dynamics affects the viscous flow itself. To do so, we consider the case where an axisymmetric elongated bubble of initial radius a_o is located on the axis of a fully viscous line vortex. For illustration, we consider the case where, at $t = 0$, the vortex line is a Rankine vortex. From there on, the vortex diffuses with time and interacts fully with the bubble. The generated flow satisfies the axisymmetric incompressible Navier-Stokes' equations in cylindrical coordinates. With all derivatives with respect to z and θ being null, the continuity and momentum equations reduce to:

$$\frac{1}{r}\frac{\partial}{\partial r}(r\varrho u_r) = 0 \tag{18.8.1}$$

$$\frac{\partial u_r}{\partial t} + u_r\frac{\partial u_r}{\partial r} - \frac{u_\theta^2}{r} = \frac{-1}{\varrho}\frac{\partial p}{\partial r} + \nu\frac{\partial}{\partial r}\left[\frac{1}{r}\frac{\partial}{dr}(ru_r)\right] \tag{18.8.2}$$

$$\frac{\partial u_\theta}{\partial t} + u_r \frac{\partial u_\theta}{\partial r} + \frac{u_r u_\theta}{r} = \nu \frac{\partial}{\partial r}\left[\frac{1}{r}\frac{\partial}{\partial r}(r u_\theta)\right] \tag{18.8.3}$$

Denoting the radius of the bubble as $a(t)$, and its time derivative, $\overset{\circ}{a}(t)$, the continuity equation leads to:

$$u_r = \frac{a(t)\,\overset{\circ}{a}(t)}{r} \tag{18.8.4}$$

Replacing u_r by its expression in (18.8.2) and (18.8.3) one obtains:

$$\frac{1}{r}\left[a\,\overset{\circ\circ}{a} + \overset{\circ}{a}^2 - u_\theta^2 - \frac{a^2\,\overset{\circ}{a}^2}{r^2}\right] = -\frac{1}{\varrho}\frac{\partial p}{\partial r} \tag{18.8.5}$$

$$\frac{\partial u_\theta}{\partial t} + \frac{a\,\overset{\circ}{a}}{r}\left(\frac{\partial u_\theta}{\partial r} + \frac{u_\theta}{r}\right) = \nu \frac{\partial}{\partial r}\left[\frac{1}{r}\frac{\partial}{\partial r}(r u_\theta)\right] \tag{18.8.6}$$

This set of coupled equations allows one to describe both the bubble dynamics and flow field modification with time accounting for the interaction with the bubble.

XVIII.8.1 Method of Solution

In order to obtain a differential equation for the bubble radius variations, similar to the Rayleigh-Plesset Equation (18.3.15), Equation 18.8.5 is integrated between $r = a(t)$ and a very large radial distance $r = R_\infty$, beyond which the vortex flow is assumed to be that of an inviscid line vortex of circulation Γ. This integration leads to a term containing u_θ^2. In order to obtain this term, a space and time integration of Equation 18.8.6 is needed. This is obtained using a Crank-Nicholson finite difference integration scheme applied to Equation 18.8.6. To apply this scheme, the domain of integration is made time independent using the variable change,

$$s = \frac{r}{a(t)} \tag{18.8.7}$$

The integration region becomes for all times $[1; s_\infty]$, with $R_\infty(t) = a(t)s_\infty$. With a, $\overset{\circ}{a}$ known at a given time step through the solution of Equation 18.8.5, Equation 18.8.6 becomes:

$$\frac{D\overline{u_\theta}}{D\overline{t}} = -\frac{s\,\overset{\circ}{\overline{a}}}{\overline{a}}\frac{\partial \overline{u_\theta}}{\partial s} - \frac{\overset{\circ}{\overline{a}}}{s\overline{a}}\frac{\partial \overline{u_\theta}}{\partial s} - \frac{\overset{\circ}{\overline{a}}}{s^2\overline{a}}\overline{u_\theta} + \frac{1}{R_e}\frac{1}{\overline{a}^2}\left(\frac{\partial^2 \overline{u_\theta}}{\partial s^2} + \frac{1}{s}\frac{\partial \overline{u_\theta}}{\partial s} - \frac{\overline{u_\theta}}{s^2}\right) \tag{18.8.8}$$

with

$$\overline{a} = \frac{a}{a_0} \quad \overline{t} = \frac{t}{a_0}\sqrt{\frac{P_\infty}{\varrho}} \quad \overline{u_\theta} = u_\theta\sqrt{\frac{P_\infty}{\varrho}} \quad R_e = \frac{a_0}{\nu}\sqrt{\frac{P_\infty}{\varrho}} \quad \overline{r} = \frac{r}{a_0} \tag{18.8.9}$$

Similarly, Equation 18.8.5 becomes:

$$\bar{a}\,\mathring{\mathring{\bar{a}}} + \mathring{\bar{a}}^2 = \frac{\mathring{\bar{a}}^2}{2\ln(s_\infty)}\left[-\frac{1}{s_\infty^2}+1\right] + \frac{1}{\ln(s_\infty)}\int_1^{s_\infty}\frac{\overline{u_\theta}^2}{s}ds$$

$$-\frac{1}{\ln(s_\infty)}\left[1-\left(\frac{\bar{\Gamma}}{2\pi\bar{a}s_\infty}\right)^2 - \overline{p_v} + \overline{p_{go}}\left(\frac{1}{\bar{a}}\right)^{2k} - \frac{1}{W_e\bar{a}} - \frac{2\,\mathring{\bar{a}}}{R_e\bar{a}}\right] \tag{18.8.10}$$

with

$$\bar{\Gamma} = \frac{\Gamma}{a_o}\sqrt{\frac{P_\infty}{\varrho}} \quad \overline{p_v} = \frac{p_v}{p_\infty} \quad \overline{p_g} = \frac{p_g}{p_\infty} \quad W_e = \frac{a_o P_\infty}{\sigma} \tag{18.8.11}$$

XVIII.8.2 Initial and Boundary Conditions

The initial conditions considered are as follows. For the bubble,

$$a(0) = a_o \qquad \mathring{a}\,(0) = 0 \tag{18.8.12}$$

For the line vortex, the equation at $t = 0$, is that of a Rankine vortex as described in §I.1.1, with

$$u_r(r, t = 0) = 0 \tag{18.8.13}$$

In addition, the following boundary condition, similar to Equation (18.4.4), is imposed at the bubble interface:

$$P(a) = p_v + p_{g_o}\left(\frac{a_o}{a}\right)^{2k} - \frac{\sigma}{a} + 2\mu\frac{\partial u_r(a)}{\partial r} \tag{18.8.14}$$

where μ is the dynamic viscosity, and the gas compression law is given by:

$$p_g = p_{g_o}\left(\frac{a_o}{a}\right)^{2k} \tag{18.8.15}$$

In addition, the following condition at infinity is imposed on the pressure at the distance, R_{inf} :

$$P(R_\infty) = p_\infty - 2\varrho\left(\frac{\Gamma}{2\pi s_\infty a(t)}\right)^2 \tag{18.8.16}$$

XVIII.8.3 Some Preliminary Results

Figures 18.8.1a and 18.8.1b illustrate both the bubble/vortex flow field interaction and a case where there is a need to include this full interaction in the dynamics. In these two figures, the bubble has an initial radius of $1mm$, while the viscous core of the vortex has an initial radius of $1cm$. The initial circulation in the vortex is 0.5 m^2/s, and the initial pressure in the bubble is 5×10^3 Pa, while the ambient pressure is 1.3×10^5 Pa. Therefore, the bubble starts its dynamics by collapsing.

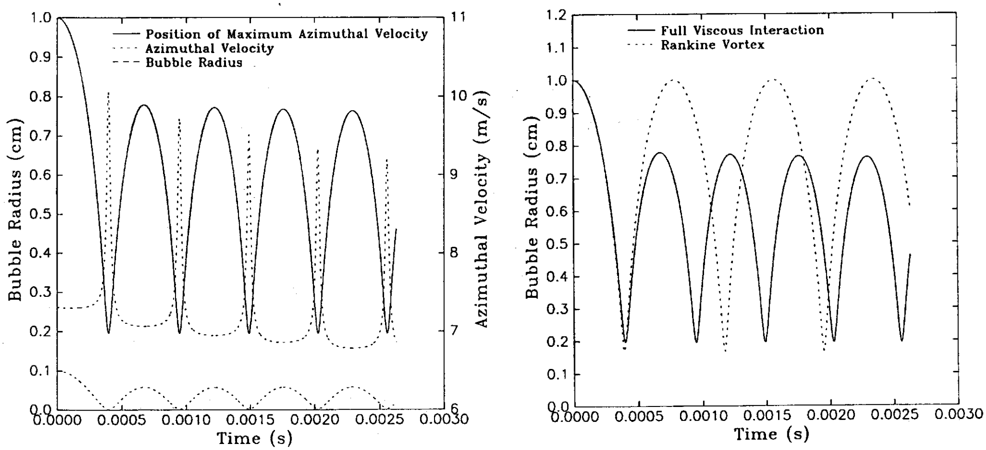

(a) (b)

Figure 18.8.1 Dynamics of the interaction between a cylindrical bubble and a line vortex. $\Gamma = 0.5$ m^2/s, $P_{go} = 5\times10^3$Pa, $P_\infty = 1.3\times10^5$Pa. a) Bubble radius, value of maximum azimuthal velocity $u_{\theta\,\max}$, and position of $R_{\theta\,\max}$. b) Bubble radius versus time with and without viscous interaction.

Figure 18.8.1a shows three characteristic quantities of the problem versus time. The first quantity is the bubble radius versus time, while the other two quantities are the maximum azimuthal velocity, $u_{\theta\,\max}$, and the radial position, $R_{\theta\,\max}$, at which this velocity occurs. In the previous sections, these two last quantities remained constant with time. A very important first result clearly shown in Figure 18.8.1a is that both the position of $R_{\theta\,\max}$, and the value of $u_{\theta\,\max}$, depend directly on the variation of $a(t)$. The viscous core (of radius $R_{\theta\,\max}$) is seen to decrease with the bubble radius during bubble collapse, and to increase with the bubble radius during bubble growth. This tendency of the viscous core to get displaced with the bubble wall corresponds to intuition, but is proven numerically, to our knowledge, for the first time here and in Desgrees du Lou et al. (1993).

Viscous effects appear more prominently when following the bubble dynamics over more than a single period of oscillation. Both maximum values of $R_{\theta\,\max}$ and $u_{\theta\,\max}$ are seen to decrease with time. Through conservation of momentum, the azimuthal velocity follows a tendency opposite to that of the core size. As the bubble wall moves inward the viscous core shrinks, simultaneously increasing the tangential velocity to a maximum when the bubble reaches maximum size. As the bubble grows again, the core expands and the tangential velocity decelerates to a minimum at the maximum bubble radius. When the fluid particles are pulled in towards the vortex axis they accelerate tangentially. This is similar to the phenomenon of vortex stretching .

Figure 18.8.1b shows the importance of the inclusion of full viscous flow/bubble interaction in the dynamics. One graph in the figure considers the case where the underlying flow field is forced to remain that of a Rankine vortex. In that case, as apparent in the figure, the bubble oscillations are repeatable with time, and no viscous decay of the amplitude of the oscillations is visible. In contrast, when the underlying flow is modified through viscous diffusion and interaction with the bubble, the bubble radius oscillations decay substantially after the first collapse, and the flow field characteristics are modified as shown in Figure 18.8.1a.

Figures 18.8.2a and 18.8.1b show, respectively, the influence on the dynamics of the initial gas pressure inside the bubble, P_{go}, and the ratio of initial core radius to initial bubble radius, R_c/a_o. For an initial pressure on the vortex axis of 7×10^5 Pa, Figure 18.8.2a shows the dynamics of the bubble and the viscous core size when the initial pressure in the bubble decreases from 5×10^5 Pa to 1.5×10^5 Pa. For $P_{go} = 5\times10^5$Pa the bubble collapse is very weak, and the core radius is seen to follow the bubble wall oscillations. For all three smaller values of P_{go}, beginning with $P_{go} = 4\times10^5$ Pa, the bubble collapse is strong enough to cause the viscous core to practically disappear (maximum azimuthal velocity at the bubble wall) during the later phases of the bubble collapse. This is followed by a much stronger rebound of the viscous core than the bubble rebound.

Figure 18.8.2b shows a behavior similar to the previous figure when the ratio, R_c/a_o, increases. Here again a strong core collapse and rebound is observed when

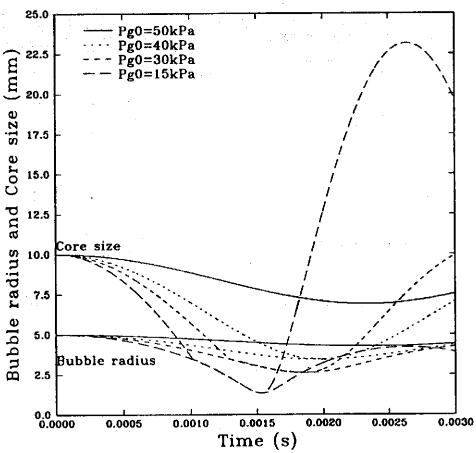

(a)

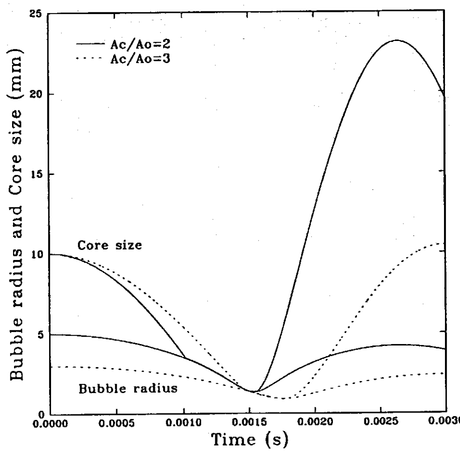

(b)

Figure 18.8.2 Dynamics of the interaction between a cylindrical bubble and a line vortex. $P_{axis} = 7\times10^5$ Pa . a) Influence of the initial bubble pressure, P_{go}, on bubble radius and position of $R_{\theta\,max}$. $R_c/a_o = 2$. b)Influence of R_c/a_o on the bubble radius and position of $R_{\theta\,max}$. $P_{go} = 1.5\times10^5$ Pa.

the initial distance between the bubble wall and the core radius is decreased.

XVIII.9 Conclusions

The study of bubble/vortex interaction is rather complex and is a subject of great interest. Due to the difficulties involved in both experimental and analytical approaches, the trend has been to address the problems by a two-pronged effort involving numerical and experimental simulations. The studies presented above addressed various aspects of the interaction problem, namely bubble capture by the vortex and bubble dynamics in the vortex flow field. Very much lacking and presently a subject of active work at our research center is the influence of the bubble's presence on the vortex behavior. It is hoped that combining a viscous solver, at least in the vortex viscous core region, with a bubble dynamics solver, such as **2DynaFS** or **3DynaFS**, would enable one to describe with some accuracy the full interaction between the bubbles and the vortex flow field. This is of great importance since it would enable one to understand the mechanics involved, potentially enabling one to manipulate the phenomena for technological advantage such as bubble drag reduction or cavitation inception delay.

Acknowledgements

This study was partially supported by the Office of Naval Research, Contract N00014-89-C-0025. The author would like to acknowledge the contributions of colleagues at DYNAFLOW, INC. especially Dr. Ramani Duraiswami and Dr. Kenneth Kalumuck for their help with the BEM code, and their review of and suggestions for the manuscript. Special thanks to Prof. Sheldon Green and Dr. Jean-Yves Billard for providing pictures to illustrate the text, and to the following ex-students at the Ecole Navale de Brest for their contributions to part of this study: Eric Delepoule, Pierre Hauwaert, Thomas Sarazin and Guillaume Desgrees du Lou. Many thanks also to the Numerical Aerodynamic Simulation (NAS) Systems Division at NASA Ames Research Center for a grant of supercomputer time.

References

Blake, J. R., Taib, B. B. and Doherty, G. 1986 Transient cavities near boundaries. Part I. Rigid Boundary. *Journal of Fluid Mechanics* **170**, 479-497.

Blake, J. R, and Gibson, D. C. 1987 Cavitation bubbles near boundaries. *Annual Review Fluid Mechanics* **19**, 99-123.

Bovis, A. G. 1980a Asymptotic study of tip vortex cavitation. *ASME Cavitation and Polyphase Flow Forum* 19-21.

Bovis, A. G. 1980b Etude asymptotique du phénomène de cavitation. Cavités non-sphériques. Thèse de Docteur Ingénieur. Université Pierre et Marie CURIE.

Chahine, G. L. 1989 A numerical model for three-dimensional bubble dynamics in complex configurations. *22nd. American Towing Tank Conference*, Newfoundland, Canada.

Chahine, G. L. 1990a Nonspherical bubble dynamics in a line vortex. *ASME Cavitation and Multiphase Flow Forum.*

Chahine, G. L. 1990b Numerical modeling of the dynamic behavior of bubbles in nonuniform flow fields. *ASME Symposium on Numerical Methods for Multiphase Flows.*

Chahine, G. L. 1991 Dynamics of the interaction of non-spherical cavities. *Mathematical Approaches in Hydrodynamics.* T. Miloh (ed.) SIAM.

Chahine, G. L. and Genoux Ph. 1983 Collapse of a cavitating vortex ring. *Journal of Fluids Engineering* **105**, 400-405.

Chahine, G. L., Perdue, T. O. and Tucker, C. B. 1988 Interaction between an underwater explosion and a solid submerged structure. *Dynaflow, Inc. Technical Report* 89001-1.

Chahine, G. L., Kalumuck, K. M., Frederick, G. S. and Watson, R. E. 1988 Development of a directed underwater destructive vortex bubble ring. *Tracor Hydronautics Inc. Technical Report* 88018-1.

Chahine, G. L. and Perdue, T. O. 1989 Simulation of the three-dimensional behavior of an unsteady large bubble near a structure. *Drops and Bubbles.* T. G. Wang (ed.) A.I.P. Conference Proceedings.

Chahine, G. L., Delepoule, E. and Hauwaert, P. 1993a Study of the interaction between a bubble and a vortical structure. *ASME Cavitation and Multiphase Flow Forum.*

Chahine, G. L., Frederick, G. F. and Bateman, R .D. 1993b Propeller tip vortex cavitation suppression using selective polymer injection. *Journal of Fluids Engineering* **115**, 497-504.

Chahine, G. L. and Duraiswami, R. 1993c Boundary element method for calculating 2-D and 3-D underwater explosion bubble behavior in free water and near structures. *Naval Surface Warfare Center, Dahlgren Division, White Oak Detachment.* Report NSWCDD/TR-93/44.

Crespo, A., Castro, F., Manuel, F. and Hernandez, J. 1990 Dynamics of an elongated bubble during collapse. *Journal of Fluids Engineering* **112**, 232-237.

Darrozes, J. S. and Chahine, G. L. 1983 Les recherches sur le phé*nomène de cavitation à l'Ecole Nationale Supérieure des Techniques Avancées. Sciences et Techniques de l'Armement* Imprimerie Nationale.

Desgrees du Lou, G., Sarazin, T. and Chahine, G. L. 1993 Viscous interaction between bubble and line vortex. *Dynaflow, Inc. Technical Report* 6.002-15.

Dvila-Martin, J., Gan-Calvo, A. M. and Lasheras, J. C. 1992 Coupled, 3-D bubbly vortical flows. *Bull. Amer. Phys. Soc., Ser. II* **37**, 1743.

Genoux, Ph. and Chahine, G. L. 1984 Simulation of a pressure field due to a submerged oscillating jet impacting a solid wall. *Journal of Fluids Engineering* **106**, 491-496.

Green, S. I. 1991 Correlating single phase flow measurements with observations of trailing vortex cavitation. *Journal of Fluids Engineering* **113**, 125-130.

Guerri, L., Lucca, G. and Prosperetti, A. 1981 A numerical method for the dynamics of non-spherical cavitation bubbles. *Proc. 2nd Int. Coll. on Drops and Bubbles* JPL Publication.

Hammitt, F. G. 1980 *Cavitation and Multiphase Flow Phenomena.* McGraw-Hill.

Higuchi, H., Arndt, R. E. A. and Rogers, M. F. 1989 Characteristics of tip vortex cavitation noise. *Journal of Fluids Engineering* **111**, 495-502.

Johnson, V. E. Jr. and Hsieh, T. 1966 The influence of trajectories of gas nuclei on cavitation inception. *Proc. 6th Symposium of Naval Hydrodynamics.*

Kalumuck, K. M. and Chahine, G. L. 1990 Cavitating vortex ring formation and dynamics. *ASME Cavitation and Multiphase Flow Forum.*

Kezios, P. and Schowalter, W. R. 1986 Rapid growth and collapse of single bubbles in polymer solutions undergoing shear. *Phys. Fluids* **29**, 3172-3181.

Kumar, S. and Williams, K. L. 1992 Study of the effect of bubbles on a two-stream mixing layer. *Bull. Amer. Phys. Soc., Ser. II* **37**, 1746.

Latorre, R. 1980 Study of tip vortex cavitation noise from foils. *International Shipbuilding Progress* 676-685.

Latorre, R. 1982 TVC noise envelope - an approach to tip vortex cavitation noise scaling. *Journal of Ship Research* **26**, 65-75.

Ligneul, P. 1989 Theoretical tip vortex inception threshold. *Eur. J. Mech. B – Fluids* **8**, 495-521.

Ligneul, P. and Latorre, R. 1989 Study of the capture and noise of spherical nuclei in the presence of the tip vortex of hydrofoils and propellers. *Acustica* **68**.

Maines, B. H. and Arndt, R. E. A. 1993 Bubble dynamics of cavitation inception in a wing tip vortex. *ASME Cavitation and Multiphase Flow Forum.*

Milne-Thomson 1968 *Theoretical Hydrodynamics*. MacMillan.

Plesset, M. S. 1948 Dynamics of cavitation bubbles. *J. of App. Mech.* **16**, 228-231.

Rayleigh, Lord. 1918 On the pressure developed in a liquid during collapse of a spherical cavity. *Phil. Mag.* **34**, 94-98.

Reutsch, G. R. and Meiburg, E. 1992 The dynamics of small spherical bubbles in vortices and mixing layers. *Bull. Amer. phys. Soc., Ser. II* **37**, 1746.

Rightley, P. M. and Lasheras, J. C. 1991 Bubbles in a two-dimensional shear layer. *Bull. Amer. Phys. Soc., Ser II* **37**, 1804.

Stewart, C. W. and Crowe, C. T. 1993 Bubble dispersion in free shear flows. *Int. J. Multiphase Flow* **19**, 501-507.

Taib, B. B. 1985 Boundary integral method applied to cavitation bubble dynamics. Ph. D. Thesis, University of Wollongong.

van Wijngaarden, L. 1980 Sound and shock waves in bubbly liquids. *Cavitation and Inhomogeneities in Underwater Acoustics*. W. Lauterborn (ed.), Springer-Verlag, 127-140.

Wilkerson, S. 1989 Boundary integral technique for explosion bubble collapse analysis. *ASME Energy Sources Technology Conference and Exhibition.*